参赛学生姓名:李涵乔

中学:北京师范大学附属实验中学

省份:北京

国家/地区:中国大陆

指导老师1姓名:卢圆圆

指导老师 1 单位: 浙江大学环境污染防治研究所

指导老师 2 姓名:杨颖

指导老师 2 单位: 北京师范大学附属实验中学

论文题目: 用多尺度电化学揭示美人蕉源纳米生物炭

活性磷异质性及释放机制

Revealing Active Phosphorus Heterogeneity and Release Mechanisms of Canna-Derived Nano-Biochar through Multiscale Electrochemistry

Abstract:

Phosphorus (P) is essential for crop growth, but excessive use of conventional chemical fertilizers has led to severe environmental issues, particularly eutrophication. Biochar and its nanoscale derivative (nano-biochar, NBC) derived from plant residues offer promising green alternatives due to their strong adsorption capacity and environmental compatibility. However, macro-scale studies often overlook the microscopic heterogeneity and kinetics that govern their dual role in regulating P release and fixation.

In this study, nano-biochar synthesized from Canna indica (CNBC) was developed as a novel slow-release P fertilizer, and its behavior was investigated through multiscale electrochemistry (cyclic voltammetry and single-entity collision electrochemistry) combined with density functional theory (DFT) calculation. CNBC produced at 500 °C is rich in oxygen-containing groups and Ca²⁺, facilitating reactive P-liable phosphate adsorption via electrostatic and complexation interactions with a slow-release effect, especially under acidic conditions. Single-particle analysis highlights heterogeneity in binding sites: most support slow release, ideal for sustained nutrient supply, while a minority strongly fix phosphate, minimizing runoff. Molecular dynamics simulations in solvation environment show gradual dissociation of the Ca-P ion pair from NBC, supported by reduced binding energy through functionalization, enabling tunable release rates.

These findings underscore the CNBC's potential as an eco-friendly fertilizer that improves P bioavailability while mitigating environmental risks and supporting sustainable waste valorization. This study offers new insights into green fertilizer design and contributes to strategies for achieving zero-growth in chemical fertilizer input under sustainable farmland management.

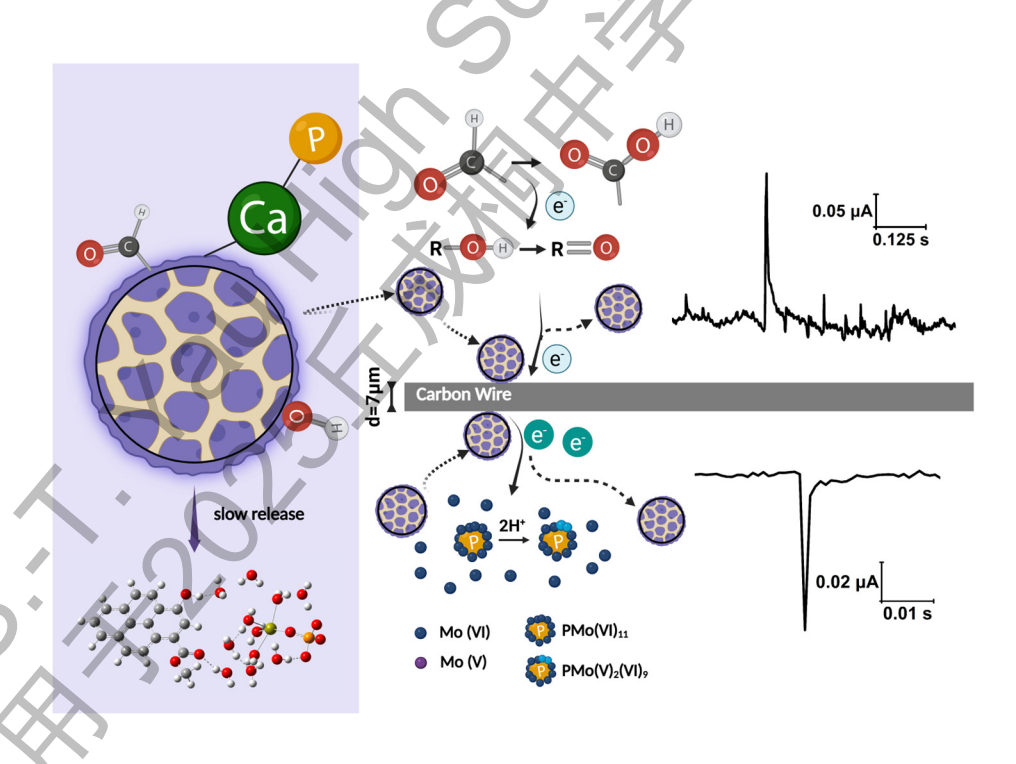
Keywords: Nanobiochar; Single-entity collision electrochemistry (SECE); Phosphorus slow-release; Green fertilizer; Waste valorization; Canna indica

摘要:

磷是作物生长的必需元素,但传统化学肥料的过度使用已导致水体富营养化等严峻环境问题。利用植物废弃物制备的生物炭和纳米生物炭(NBC)因其高吸附能力和环境友好性,成为具有潜力的绿色替代品。然而,宏观研究方法难以充分揭示其调控磷释放与固定的非均质性和微观动力学机制。本研究以美人蕉(Canna indica)为原料合成纳米生物炭

(Nano-biochar, NBC),并将其作为一种新型缓释磷肥,通过多尺度电化学方法(包括循环 伏安法和单颗粒碰撞电化学)与密度泛函理论(Density Functional Theory, DFT)计算相结 合,系统探究其行为机制。结果表明,500 ℃ 热解制备的美人蕉源纳米生物碳(Canna indica-derived nano-biochar, CNBC)富含含氧官能团和 Ca^{2+} 离子,可通过静电和络合作用有效吸附磷并表现出缓释特性,尤其在酸性条件下更为显著。单颗粒电化学分析揭示了结合位点的显著异质性:大多数位点支持缓释行为,有利于持续供养,少数位点则强吸附并固定磷酸盐,从而减少养分流失。分子动力学模拟表明,在溶剂化环境中,Ca-P 离子对逐渐从 NBC 表面分离,且含氧官能团修饰显著降低了 NBC 与磷酸根离子的结合能,从而实现可控的磷释放速率。这些发现凸显了 CNBC 作为一种环境友好型肥料的潜力,可提高磷的生物有效性、降低环境风险并支持农业废弃物的资源化利用。该研究为绿色缓释磷肥的设计提供了新思路,并为推动化肥零增长目标下的农田可持续管理提供了理论与数据支持。

关键词: 纳米生物碳, 单颗粒碰撞, 缓释磷, 绿色肥料, 废物资源化利用, 美人蕉



Graphical Abstract

Catalogue

Catalogue
1. Introduction5
2. Method6
2.1 Synthesis and Characteristics of Nano-biochar6
2.2 Working Electrode Preparation and Characterization
2.3 The Modification and Electrochemical Behavior of CNBC on GCE7
2.4 Single Entity Collision of Nano-biochar at Carbon Micro-wire Electrode
2.5 Species Distribution of Molybdate/Phosphorus Containing Compounds9
2.6 Quantum Chemistry and Ab Initio Molecular Dynamics Calculations10
2.7 Data Processing
3. Results and Discussion
3.1 Morphology Features and Characterization of Nano-biochar
3.2 First Principle Understanding and Modulating of NBC Molecular Structure14
3.3 Theoretical Calculation on Species Distribution as a Function of pH20
3.4 Electrochemical Behavior of Mo (VI) in the Solution Phase in CV21
3.5 Electrochemical Identification of Surface-Bound Phosphate on CNBC23
3.6 Electrochemical Identification of Phosphate Loaded by Single CNBC Particle25
4. Environmental Implications
5. Conclusions 31
Reference
Appendix35

1. Introduction

Phosphorus (P) is one of the most crucial nutrient elements for crop growth in soils, as it appears as the essential component of ATP, nucleic acids, coenzymes, etc., and drives biochemical processes, such as photosynthesis, in plants ^{1, 2}. The natural availability of P in soil is extremely limited, which has historically led to the widespread application of chemical P fertilizers. While effective in the short run, the excessive use of these fertilizers has contributed to severe environmental challenges, including aquatic eutrophication, nutrient runoff, and soil degradation ³⁻⁵. Recent reports indicate that more than half of China's major lakes have experienced increasing eutrophication from 2012 to 2020, which directly contaminates water and food, exposes toxins to humans' and animals' health, and damages ecological biodiversity ⁶. Therefore, a greener and more environmentally friendly P fertilizer should be applied to substitute conventional chemical fertilizer.

Biochar, a carbon-dense substance derived from the pyrolysis of biomass, has emerged as a promising candidate ⁷ due to its ability to adsorb and gradually release phosphate through electrostatic interactions, ion exchanges, precipitation, and pore-filling at a slower rate ⁸. Its high porosity and adsorption capacity enable agricultural application and environmental remediation, including nutrient supply, soil and water retention ⁹. However, the effect of biochar on soil P dynamics remains contentious. Some indicate biochar significantly increases the P availability of soil for plants ^{10, 11}. While other studies indicate strong adsorption ability and P removal efficiency of biochar ^{8, 12}.

Recent studies state that nano-biochar (NBC), obtained by downsizing bulk-biochar to the nanometer scale (1-1000 nm), has been proposed as a more effective fertilizer material owing to its higher surface area, improved colloidal stability and enriched availability of labile P ⁹. For example, Liang et al. demonstrated that micro- and nano-sized manure-derived biochar reduced colloidal phosphorus release by 45% under single intermittent anoxic treatment ¹³. Notably, NBC derived from *Canna indica* is particularly promising ¹⁴, not only because it is a renewable and low-cost feedstock with high mineral content, but also due to its capacity to bind phosphate ions via cation—anion interactions (e.g., Ca²⁺/Mg²⁺ with PO₄³⁻) ^{8,15}.

Despite the progress made, the current understanding of P bioavailability regulation by NBC remains fragmented, in part because most agricultural studies employ bulk-scale spectroscopic or

chemical extraction techniques ¹⁶⁻¹⁸. These methods provide macroscopic information, obscuring the intrinsic heterogeneity among particles and leaving critical questions unresolved. Since P adsorption and release are governed by surface functional groups, charge distribution, and interfacial redox processes ⁸, direct electrochemical characterization becomes indispensable. Electrochemical methods are uniquely suited for this task because they can probe interfacial reactions in real time with high sensitivity, offering quantitative insight into phosphate bonding, redox activity, and dynamic electron transfer processes at the biochar surface.

However, conventional ensemble electrochemical techniques, such as cyclic voltammetry (CV) or impedance spectroscopy, still suffer from the limitation of averaging responses over large populations of particles. This averaging effect conceals particle-to-particle variability in adsorption capacity and surface activity that control the performance of NBC as a P carrier. To overcome this barrier, single-particle collision electrochemistry (SPCE, also called nano-impact) has recently emerged as a powerful tool ^{19, 20}. By detecting the stochastic electrochemical signals generated when individual NBC particles collide with a microelectrode, SPCE captures heterogeneity at the single-entity level. Each collision event not only reveals heterogeneity in phosphate binding capacity but also uncovers dynamic electron-transfer processes that cannot be captured by traditional voltammetry, allowing a more precise understanding of the relationship between structural features and functional performance in soil environments.

In this study, this experiment employed *Canna indica*-derived nano-biochar (CNBC) as a sustainable P carrier for fertilization. The related phosphate interaction mechanisms are systematically investigated using CV for characterizing the bulk electrochemical response, SPCE for particle-level heterogeneity and density functional theory (DFT) calculations for elucidating the underlying mechanism. Together, these approaches not only validate NBC as a potential green phosphorus fertilizer but also pave the way for rational tuning of its molecular and surface properties to optimize phosphorus regulation efficiency.

2. Method

2.1 Synthesis and Characteristics of Nano-biochar

As a comparison, the NBC was produced from locally collected Canna indica and Maize straw.

The material was respectively air-dried, cut into small pieces, and pyrolyzed in a muffle furnace

under oxygen-limited conditions. The furnace was heated at a rate of 10 °C/min to 500 °C, where the temperature was maintained for 2 h. After cooling, the resulting biochar was ground and sieved to < 2 mm. To further reduce particle size before field application, the biochar was milled using a planetary ball mill (operating parameters: forward rotation for 5 min, reverse rotation for 5 min, with 5 min intervals, for a total of 2 h; rotation speed: 400 rpm; ball-to-powder ratio; 20:1), achieving a sub-micron particle size.

The produced Canna indica-derived nano-biochar (CNBC) and Maize straw-derived nano-biochar (MNBC) were then comprehensively characterized. Surface morphology and elemental distribution were assessed via scanning electron microscopy coupled with energy-dispersive X-ray spectroscopy (SEM-EDS, JSM-7500F, Japan Electronics Co., Ltd., Japan). Chemical composition and surface functional groups were analyzed by Fourier transform infrared spectroscopy (FTIR; Nicolet IS50, Thermo Fisher Scientific Inc., USA) across the wavenumber range of 400–4000 cm⁻¹ with a resolution of 2 cm⁻¹, as well as by X-ray photoelectron spectroscopy (XPS; K-Alpha, Thermo Fisher Scientific Inc., USA).

2.2 Working Electrode Preparation and Characterization

All electrochemical experiments were conducted in a Faraday cage with an EC-lab potentiostat (Biologic Science Instruments SP-200, France) at 298K. A standard three-electrode system includes a carbon macro or micro-disc electrode as the working electrode, an Ag/AgCl reference electrode, and a graphite counter electrode. Prior to each cyclic voltammetry (CV) scan, the glassy carbon electrode (GCE, diameter of 3.02 ± 0.005 mm) or carbon fiber electrode (CFE, diameter of $5.0 \, \mu m$) was respectively polished on a soft suede pad using alumina slurries with progressively smaller particle sizes (1.0, 0.3, and 0.05 μm). Then the electrode was rinsed thoroughly with ultrapure water and dried under a stream of nitrogen gas. (Specific figures and testing principles of the working electrode are seen in the appendix).

2.3 The Modification and Electrochemical Behavior of CNBC on GCE

The NBC as prepared was suspended in a 1:1 (v/v) ethyl alcohol/water mixture and stirred vigorously. Subsequently, $0.8~\mu L$ of a $2.5~g \cdot L^{-1}$ CNBC suspension was drop-cast onto the pretreated GCE and then dried under nitrogen gas for 10-15 minutes.

Ammonium molybdate tetrahydrate (AMT) was dissolved in a 0.05 M K_2SO_4 solution, preparing an 8 mM ammonium permanganate K_2SO_4 stock solution for the cell (pH = 5.1, without

adjustment). Working solutions at pH = 3.50 and 7.08 are obtained by adding 0.5 M H₂SO₄ and 0.5 M KOH to adjust, respectively. The GCE was first placed in a 0.05 M K₂SO₄ solution (blank solution without Mo (VI) and phosphate) for CV at 50 mV/s to compare with the CV of the experimental groups in the presence of Mo (VI). For the CV of Mo (VI) reduction and oxidation in the presence and absence of phosphate from NBC, the working macroelectrode was first placed in 8 mM Mo (VI))/K₂SO₄ stock solution at pH = 3.50, 5.12, and 7.08, respectively, to test CV. Accordingly, the NBC-modified GCE was then scanned in 8 mM Mo (VI) K₂SO₄ stock solution at pH = 3.50, 5.12, and 7.08, respectively.

The potential window was set from 0.6 V to -0.2 V, -0.6 V to -0.3 V, and 0.6 V to -0.8 V, at pH = 3.50, 5.12, and 7.08, respectively, due to the translation of CV curves resulting from pH changes. The voltammograms were recorded at different scan rates (25, 50, 100, 200, and 400 mV s⁻¹) for each group.

Each time before CV scanning, the GCE was polished in the method mentioned earlier, cleared by ultrasound for ten seconds, and dried with nitrogen current. For biochar-modified groups, the working electrode was polished and then remodified after each scan.

2.4 Single Entity Collision of Nano-biochar at Carbon Micro-wire Electrode

The carbon fiber micro-wire electrode (7 µm diameter and approximately 1 mm in length) used for nano-impact experiment was fabricated as follows: A single carbon fiber (7 µm diameter) was stuck to a conductive copper wire by using silver explosive (RS Components Ltd.), followed by a 20-minute heating in the oven at 358 K. This connection was carefully threaded within a plastic pipette tip, enabling only the carbon fiber micro-wire to protrude from the end. To prevent electrical leakage, the gap between the carbon fiber, copper wire, and the pipette tip was sealed with cyanoacrylate adhesive. The prepared microelectrode was then placed in the heating in the oven at 358K overnight to ensure the adhesive fully dried. Before the first use in nano-impact experiments, each fresh carbon fiber microelectrode was trimmed to approximately 1 mm.

Nano-impact experiments were supported by chronoamperometry (CA), setting the potential range from 0.6 V, 0.4 V, 0.2 V, 0 V, -0.2 V, -0.4 V to -0.6V with a sensitivity of 100 nA, sampling interval time (d_t) of 0.001 s. To investigate the electrochemical peaks and charge in the presence of NBC at different pH, was performed in one group with Mo (VI) and CNBC and another group with NBC but without Mo (VI). In the first group, A 0.5 mL 0.1 g·L⁻¹ NBC solution was added to a 0.05

M K_2SO_4 solution, forming a 5 μ g·L⁻¹ NBC suspension in the cell at pH = 1.87 and pH = 4.94. In the other group, CA is tested in the cell of 5 mM Mo (VI) in K_2SO_4 solution at pH = 1.87 and pH = 4.94. The pH = 1.87 cell solution is adjusted by a small addition of 0.5 M H_2SO_4 .

2.5 Species Distribution of Molybdate/Phosphorus Containing Compounds

In order to better understand the electrochemical behavior with the involvement of Mo (VI)/P species and complexes during reactions, theoretical species distribution using Hydra/Medusa ²¹, software was conducted based on the chemical reaction equations between speciation of Mo (VI) and phosphate (P) below.

Mo (VI) oxoanions are polymerized into dimolybdate (Eq. (1)), heptamolybdate (Eq. (2)), and Octamolybdate (Eq. (3)) as acidity enhances. Meanwhile, Mo (VI) is protonated forming molybdic acid (Eq. (4-6)).

$$2M_0O_4^{2-} + 2H^+ \to M_{02}O_7^{2-} + H_2O$$
 (1)

$$7 \text{ MoO}_4^{2-} + 8 \text{H}^+ \rightarrow \text{Mo}_7 \text{O}_{24}^{6-} + 4 \text{H}_2 \text{O}$$
 (2)

$$8 \text{ MoO}_4^{2-} + 10 \text{H}^+ \rightarrow \text{Mo}_8 \text{O}_{26}^{4-} + 5 \text{H}_2 \text{O}$$
(3)

$$M_0O_4^{2-} + H^+ \rightarrow HM_0O_4^{-} \tag{4}$$

$$M_0O_4^{2-} + 2H^+ \rightarrow H_2M_0O_4$$
 (5)

$$M_0O_4^{2-} + 3H^+ \rightarrow H_3M_0O_4^+$$
 (6)

With H⁺, phosphate (PO₄³⁻) ions are protonated, forming polyprotic acid (Eq(7), Eq(8), Eq(9)).

$$PO_4^{3-} + H^+ \to HPO_4^{2-}$$
 (7)

$$HPO_4^{2-} + H^+ \rightarrow H_2PO_4^{-}$$
 (8)

$$H_2PO_4^- + H^+ \rightarrow H_3PO_4$$
 (9)

Though phosphate is electrochemically inactive, the complex formed by the reaction between phosphate and Mo (VI), is electroactive. As Eq. (10) shows, PMo₁₂O₄₀³⁻, the well-known Keggin anion of the phosphomolybdate complex, appears in acidic aqueous solutions. However, when pH changes, the polyoxomolybdate ions appear in various forms ²².

$$7H_3PO_4 + 12Mo_7O_{24}^{6-} + 51H^+ \rightarrow 7[PMo_{12}O_{40}]^{3-} + 36H_2O$$
 (10)

Since pH and proportion of concentration of Mo (VI) and PO₄³⁻ in aqueous solution affect the fraction of concentration of polymerized Mo (VI) oxoanions and polyprotic acid in multiple structures, the speciation distribution is calculated and graphed to analyze the predominant pattern of complex and electrochemical reactions under different conditions.

According to the equations of phosphate and Mo (VI), the following equations forming a complex of PO₄³⁻ and Mo (VI) are considered in speciation distribution.

$$2PO_4^{3-} + 5M_0O_4^{2-} + 10H^+ \rightarrow P_2M_0 + O_{23}^{6-} + 5H_2O$$
(11)

$$2PO_4^{3-} + 18M_0O_4^{2-} + 36H^+ \rightarrow P_2M_{018}O_{62}^{6-} + 18H_2O$$
 (12)

$$PO_4^{3-} + 11M_0O_4^{2-} + 18H^+ \rightarrow PM_{011}O_{39}^{7-} + 9H_2O$$
 (13)

$$PO_4^{3-} + 12M_0O_4^{2-} + 24H^+ \rightarrow PM_{012}O_{40}^{3-} + 12H_2O$$
 (14)

2.6 Quantum Chemistry and Ab Initio Molecular Dynamics Calculations

DFT calculations of molecular structure modified with various oxygen-containing functional groups were conducted by Gaussian 16. A Ca²⁺ was added to better simulate the attraction and bonding between PO₄³⁻ and NBC. B3LYP functional with 6-31G* basis set was used to describe the electronic structure, compute the bonding energy, and surface electrostatic potential. The bonding energy between phosphate and biochar equals the energy of biochar with Ca²⁺ and phosphate minus the sum of the energy of phosphate and Ca²⁺. The long-range interaction was accounted for by applying Grimme's D3BJ dispersion correction ²³. After optimization, frequency calculation was performed to ensure no imaginary frequency was present.

According to the position of peaks in Infrared spectroscopy, the functional groups containing C=C, C=O, -OH, C-H, -CH₂, and C-O are modified around the edge of the graphene structure of NBC $^{24-26}$. Therefore, function groups, including aldehyde, carboxylic acid, methyl formate, etc., are modified at the edge of biochar for bonding energy calculations, respectively.

To further investigate the molecular dynamics of NBC with phosphate in a solvation environment, we conducted ab initio molecular dynamics (AIMD) simulations of the structure with the modification best-fitted to experimental results. The calculation was set based on software CP2K using DZVP-MOLOPT-SR-GTH as basis set and GTH-PBE as pseudopotential with Grimme's D3 dispersion correction with BJ damping. The simulation was performed for 10000 steps with a step size of 1fs (10⁻¹⁵ s) at the NVT ensemble. The canonical sampling through velocity rescaling (CSVR) thermostat was applied to control the temperature of the simulation at 298 K.

2.7 Data Processing

Data from CV and CA are collected through EC-Lab, and peaks in single-entity collision data are processed and analyzed by Signal Counter. Simulation of Mo/P species in the solution under different pH is conducted by Hydra/Medusa. Graphs and corresponding data analysis, including

linear regression, are completed by Origin. DFT calculations and visualization are performed by Gaussian 16W and GaussView 6.0. AIMD simulation is completed on the software CP2K. Results of AIMD are visualized through OVITO and VMD.

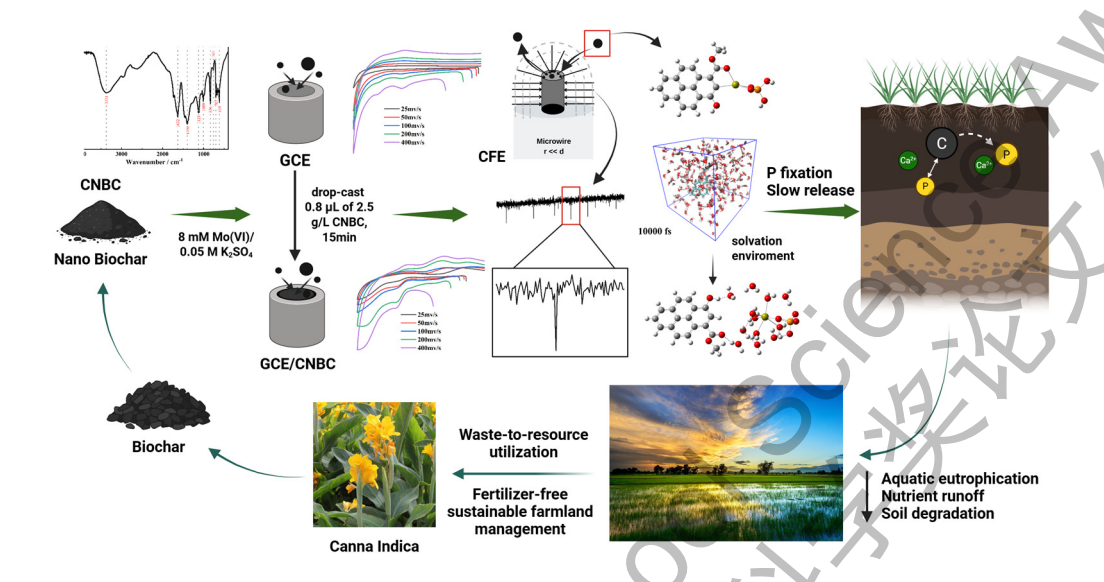


Figure. 1 The Logic Flow Chart of the Experiment

3. Results and Discussion

3.1 Morphology Features and Characterization of Nano-biochar

The SEM characterization of samples of CNBC and MNBC is shown in Figure. 2. According to Figure. 2 (a) and (c), both types of NBC exhibit granular crystalline structures formed under high-temperature pyrolysis. Figure. 2 (b) and (d) further demonstrate that NBC particles adhere to the surface of these crystals.

Figure 3 (a) compares the FTIR spectra of NBC derived from two plant sources. The CNBC shows more pronounced and distinct peaks in the range of 1500–500 cm⁻¹, particularly associated with P–O stretching and M–O coordination bonds in the fingerprint region. This suggests that CNBC has a stronger capacity to bind phosphate, making it a suitable carrier of phosphate in soils and a promising material for electrode modification in electrochemical applications. The M–O vibrations further imply the presence of metal ions, such as Ca²⁺ within the material ¹⁴. Therefore, CNBC was selected for subsequent experiments.

As shown in Figure. 3 (b), the FTIR spectra of CNBC and its original bulk biochar (CBC) reveal broad –OH stretching peaks at 3426 and 3371 cm⁻¹. Multiple peaks between 1700 and 500 cm⁻¹ indicate the presence of C=O, C-O, C-H, and C=C functional groups, suggesting that carbonyl

groups such as aldehydes, ketones, carboxylic acids, and alkyl esters are likely present on the surfaces of both CBC and CNBC. The broad absorption band from 1600 to 800 cm⁻¹ indicates an amorphous phase. Peaks near 1000 cm⁻¹ and within 700–560 cm⁻¹ confirm the presence of inorganic salts such as phosphate. Compared with BC, NBC exhibits sharper and more distinct splitting peaks, reflecting stronger vibrational coupling of P–O–C, higher PO₄³⁻ content, and an increased degree of crystallinity. These features enhance its phosphate-loading capacity, making CNBC more suitable for electrode modification and field applications.

As shown in Figure. 3 (c), CNBC samples were pyrolyzed at multiple temperatures (300, 400, and 500 °C) to optimize thermal treatment conditions. The peak distribution and intensities of oxygen-containing groups were generally consistent across the three temperatures. However, NanoBC-500 °C displayed sharper, denser, and more distinct splitting peaks, indicating a higher concentration of PO₄³⁻ and was therefore selected for electrode modification. The right-shift of the C–O peak at 500 °C can be explained by two possible mechanisms: (i) decarboxylation of carboxylate groups (R–COO⁻), releasing CO₂ and forming C–O–C or –COOR structures, which reduce polarity and hydrogen bonding, thereby shifting the symmetric stretching from ~1400 cm⁻¹ to ~1200 cm⁻¹; or (ii) partial graphitization of the carbon matrix at elevated temperatures, with residual oxygen incorporated into the ordered sp² carbon skeleton as symmetric C–O–C, which restricts vibration and lowers frequency.

The surface chemical states of CNBC were further investigated by X-ray photoelectron spectroscopy (XPS), with spectra shown in Figure. 4 (a–d). The C 1s spectrum (Figure. 4 (a)) reveals three peaks at 284,8, 288.0, and 293.3 eV, corresponding to C–C, C–O–C, and O–C=O bonds, respectively. The high-resolution O 1s spectrum (Figure. 4 (b)) is deconvoluted into three peaks: 531.0 eV (O–I), assigned to lattice oxygen (O²- in metal–oxygen frameworks); 532.2 eV (O–II), the most intense peak, attributed to surface-adsorbed oxygen species active in oxidation reactions; and 533.6 eV (O–III), which may be associated with oxygen in carbonyl groups (–COOH and –C=O) or phosphate (PO4³-). The P 2p spectrum exhibits a spin–orbit doublet, with P 2p_{1/2} and P 2p_{3/2} separated by 1.09 eV. Similarly, the Ca 2p spectrum shows two peaks (Ca 2p_{1/2} and Ca 2p_{3/2}) with a splitting energy of 3.63 eV.

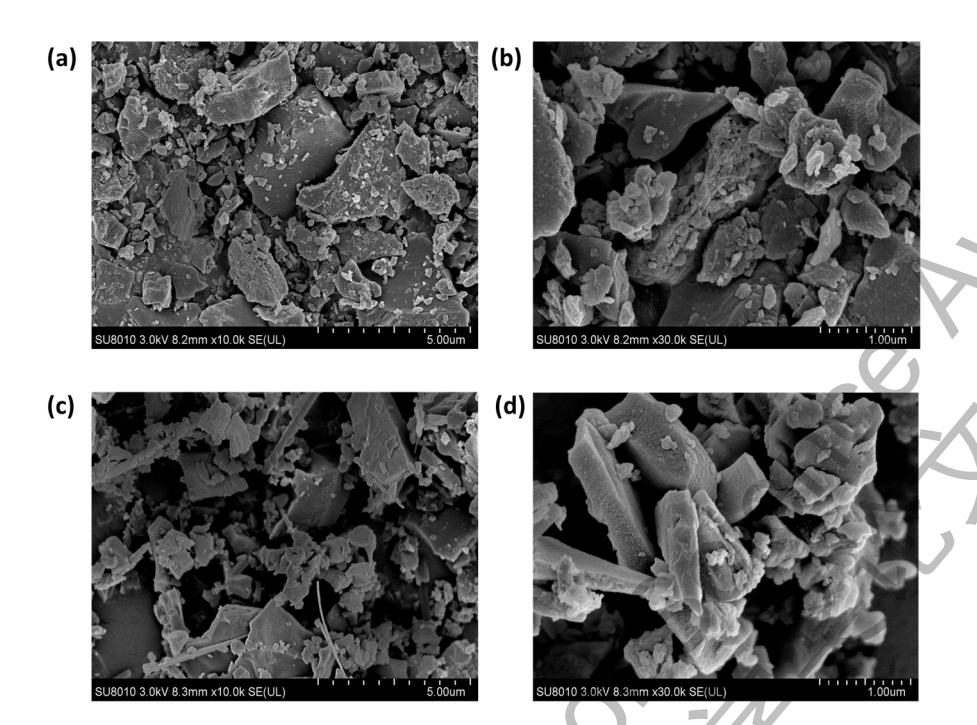


Figure. 2 Scanning electron microscope (SEM) images of biochar from corn straw at 10 k (a) and 30 k (b) and from canna indica leaves at 10 k (c) and 30 k (d).

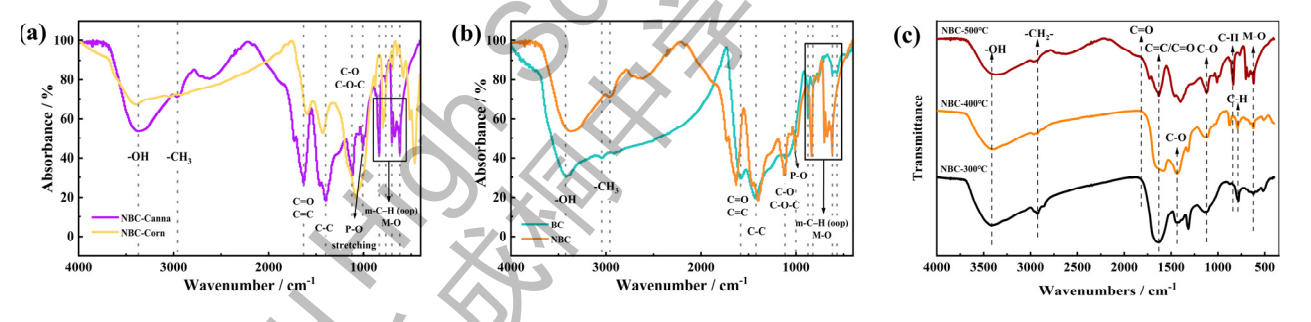


Figure. 3 Fourier-transform infrared spectroscopy (FTIR) of NBC (CNBC) made from canna and corn (a). FTIR of canna-sourced biochar (BC) and CNBC (b). FTIR of CNBC at different pyrolysis temperatures of 300, 400, and 500 °C, respectively (c).

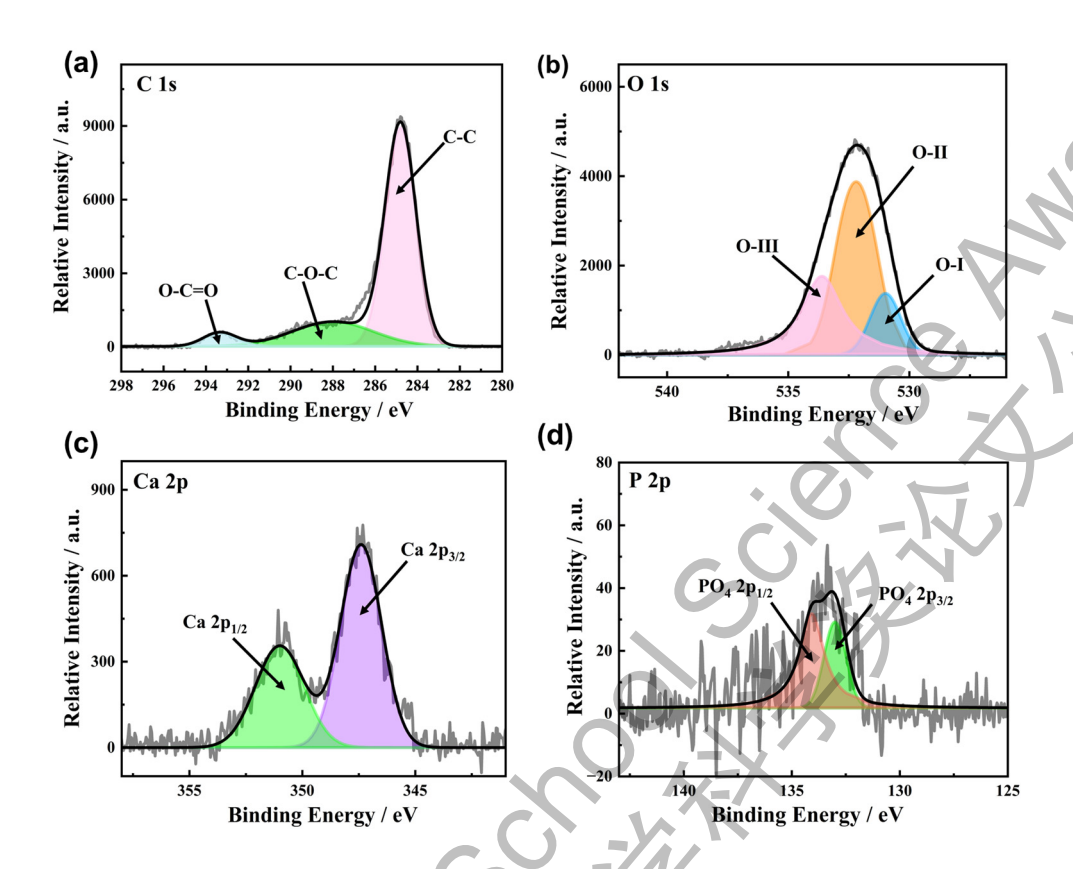
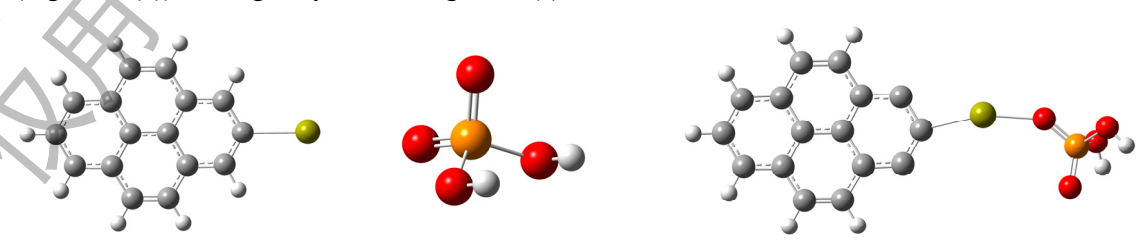


Figure. 4 The X-ray photoelectronic spectroscopy (XPS) peaks of C 1s (a), O 1s (b), Ca 2p (c), P 2p (d) for CNBC.

3.2 First Principle Understanding and Modulating of NBC Molecular Structure

The nature, especially electronegativity, of these essential oxygen-containing functional groups marks the electron motions between molecules, which dominate the bonding and dynamics of NBC and phosphate. To better explore the structure and energy of the combination of biochar and phosphoric acid from a microscopic perspective, DFT calculation is conducted.

To optimize the adsorbent capacity of biochar for phosphate adjustment in soil, factors at the molecular structure level need to be considered, such as hydrophobic attractions, electrostatic interactions and surface modification⁸. The bonding between CNBC (Figure. 5 (a)) and phosphate (Figure. 5 (b)) is bridged by Ca²⁺ as Figure. 5 (c) shows.



(a) NBC (with Ca^{2+}) (b) Phosphate($H_2PO_4^-$) (c) NBC+P

Figure. 5 Molecular models of NBC with Ca (charge = +1), phosphate (Charge = -1) and bonding configurations before optimization computations (Charge = 0). Grey atoms represent C; white atoms represent H; red atoms represent O; yellow atoms represent Ca; orange atoms represent P.

Structural optimization and frequency calculation are performed for 13 different surface modifications, including C=O, C-O, etc. Under the current precision achieved by quantum calculations, the Hartree energy of the most stable geometric configuration is concluded. The bonding energy between NBC with Ca²⁺ and phosphate is calculated as follows.

$$E_B = E_{NBC+P} - (E_{NBC} + E_P) \tag{15}$$

The configurations after frequency computation and optimization are shown in Figure. 6, and the bonding energy calculated is listed in Table 1.

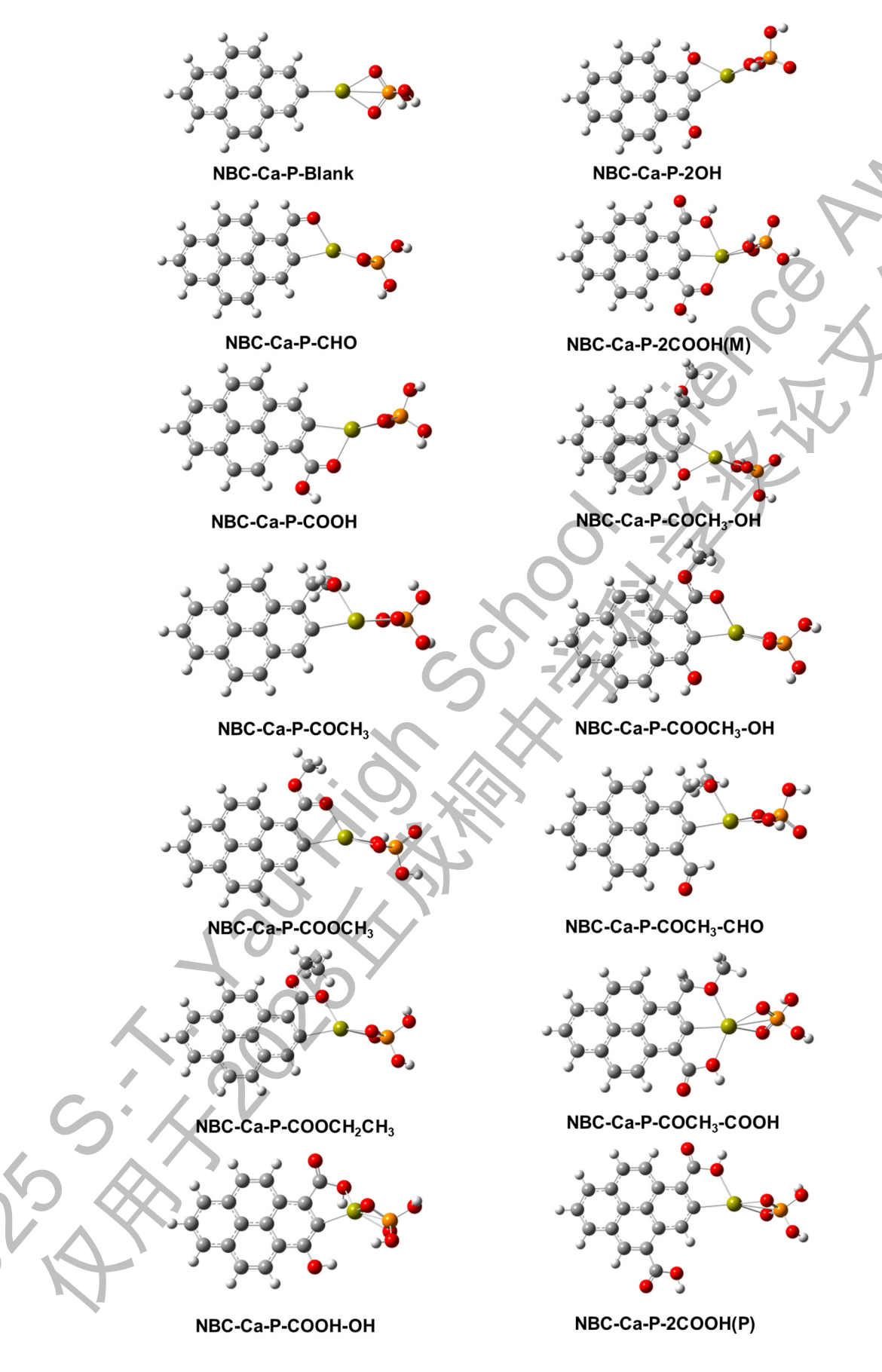


Figure. 6 Optimized structures modified NBC to evaluate its bonding energy to phosphate.

Table. 1 The calculated bonding energy. Structures in moderate bonding energy between -720 kJ·mol⁻¹ and -680 kJ·mol⁻¹ are marked in blue. The modification of "Methyl Ester + Hydroxyl" is selected to perform AIMD simulation, marked in red.

Modification	$E_B/ \text{kJ-mol}^{-1}$
NBC-Ca-P-blank (none)	-750.943
NBC-Ca-P-CHO	-703.952
NBC-Ca-P-COOH	-707.320
NBC-Ca-P-COCH ₃	-720.779
NBC-Ca-P-COOCH ₃	-678.904
NBC-Ca-P-COCH ₂ CH ₃	-702.366
NBC-Ca-P-COOH-OH	-682.462
NBC-Ca-P-2OH	-738.952
NBC-Ca-P-2COOH(M)	-662.361
NBC-Ca-P-COCH ₃ -OH	-663.012
NBC-Ca-P-COOCH ₃ -OH	-698.257
NBC-Ca-P-COCH ₃ -CHO	-690.230
NBC-Ca-P-COCH ₃ -COOH	-700.494
NBC-Ca-P-2COOH(P)	-807.040

When there is no any modification, NBC with Ca²⁺ initially binds with negatively charged phosphate with high bonding energy due to electrostatic attraction. The introduction of new electronegative functional groups, such as aldehyde, methyl acid, ester, etc., disperses and neutralizes the local positive charge of Ca²⁺ on its ortho position. This competition between the negatively charged modified functional group and anionic phosphate significantly reduces the bonding affinity. Based on the difference of this affinity among various configurations, the tradeoff between the two functions of NBC—supplementing P as released fertilizers and preventing P runoff by absorbents—can be balanced. In order to achieve NBC's slowly-released property, structures in Table 1 in moderate bonding energy between -720 kJ·mol⁻¹ and -680 kJ·mol⁻¹ are considered as a more ideal model of P fertilizers. Generally, the more oxygen-containing functional groups modified to NBC, the more the repulsion forces between NBC and phosphate with metal ions, the more dominant its releasing effect is. Conversely, reducing oxygen-containing functional groups can enhance P absorption and fixing ability. Through controlling pyrolysis temperature and selecting different raw materials, NBC's property of adsorption or release can be adjusted with different

concentrations of oxygen-containing functional groups. Therefore, the slow-releasing rate could be regulated by NBC modifications.

FTIR can be mapped based on the frequency calculations. Each structure's generated FTIR is compared with the experimental FTIR. The following figure shows the lab FTIR and the NBC modified with -COOCH3 and -OH, of which the theoretical FTIR best matches lab results.

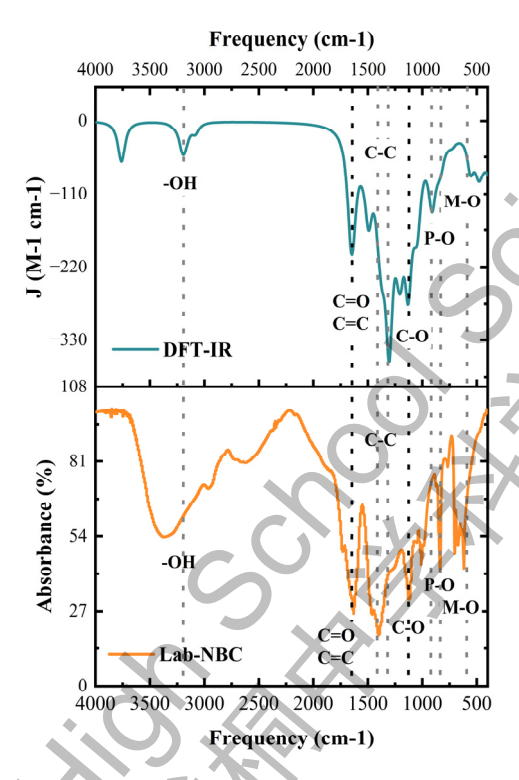


Figure. 7 Comparison of FTIR tested in lab (below) and simulated by DFT computations (above) of vibrance and frequency. Black and grey lines mark peaks appearing at close frequency.

As Figure. 7 shows, most peaks appear from 1700 cm⁻¹ to 800 cm⁻¹ in the experimental FTIR also exhibit at close frequency in the IR simulated by DFT computation. The match of peaks in this range indicates this theoretical model has similar oxygen-containing functional groups as the cannasourced NBC used for lab experiments. Based on the surface property similarity between this model and experiment material, we choose this molecular structure to examine its dynamic interaction with phosphate through CPMD. The ab initio simulation is performed for 10000 steps at 1 fs per step. The following figures show motions of molecules at different steps and the process of molecular dynamics within mesh.

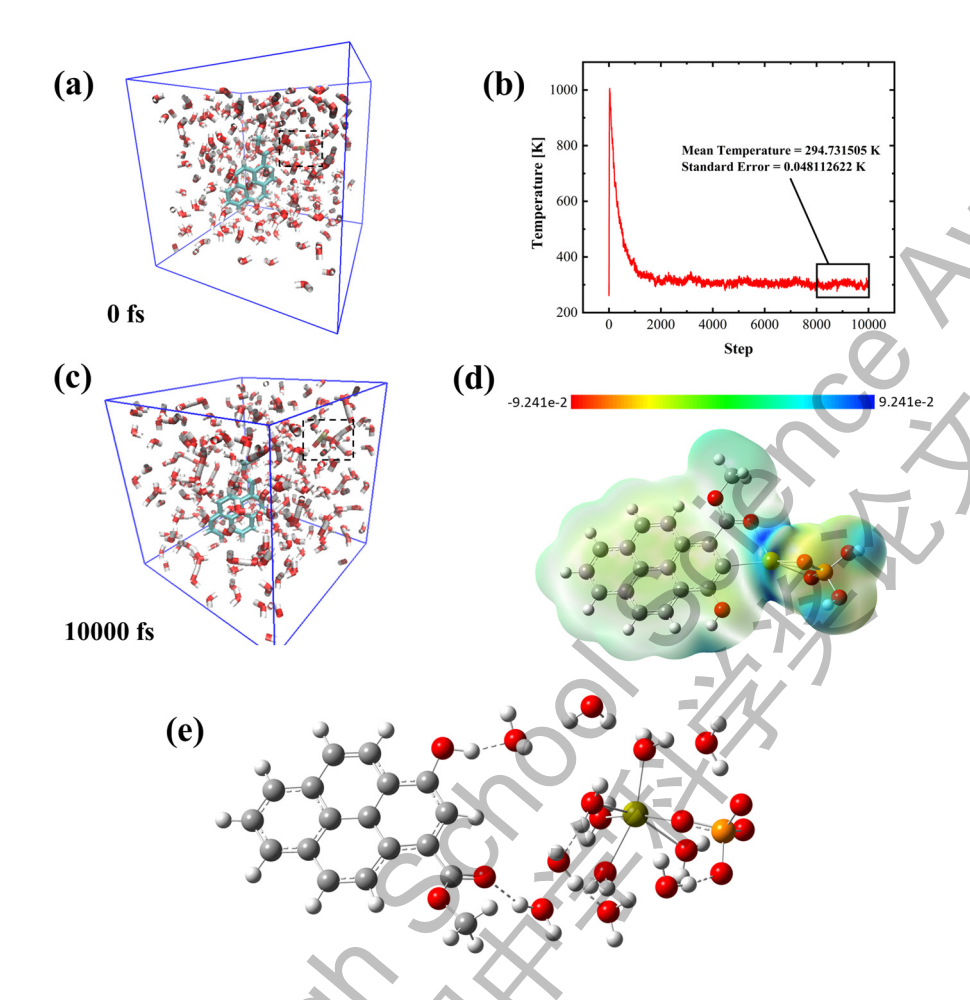


Figure. 8 (a) The initial configuration of the system for AIMD simulation. The box dimensions are 20Å×20Å×20Å with periodic boundary condition; (b) temperature profile in the system (NVT ensemble) from 0 fs to 10000 fs and mean temperature and standard error of temperature from 9800 fs to 10000 fs; (c) A snapshot of the system at 10000 fs (the part of Ca and phosphate is framed); (d) Electrostatic potential figure of NBC-Ca-Phosphate complex at initial after structural optimization; (e) solvated structure of NBC-Ca-Phosphate complex obtained from AIMD calculation at 298K. The solvation structure was stabilized by many hydrogen bonds, shown in dashed lines. Ca is in yellow, P is orange, carbon is grey, oxygen is red, and hydrogen is white.

According to Figure. 8 (b), the system reached equilibrium after 2000 fs, as evidenced by the stabilization of the temperature around 298 K. As Figure. 8 (a) and Figure. 8 (c) shows, Ca²⁺ and phosphate detach from NBC from 0 fs to 10000 fs, forming a contact ion pair at a stable distance. As the surface electrostatic potential visualized in Figure (d), the O from NBC disperses the nucleophilicity of O from phosphate, therefore weakening the attraction between phosphate and NBC. Although carboxyl is still being attracted in the direction of phosphate, the steric hindrance

between the O in H₂O and the electronegative hydroxyl and methyl acid keeps a certain distance between P and NBC, confirming that P could be steadily released from NBC instead of being strongly absorbed and difficult to separate. Therefore, CNBC has the potential of being a P fertilizer from a micro perspective.

Despite the separation between phosphate and NBC discussed above, the general process is slowly released in soil since the material is difficult to dissolve in water, as Figure. 8 (e) indicates. Traditional soluble P fertilizer quickly releases a large amount of phosphate in a short time, causing an imbalanced nutrition supplement, whereas the NBC in this study can release P for plants continuously and uniformly in the long term. Additionally, the insolubility of NBC also prevents runoff and significant loss of P, reducing eutrophication of water.

3.3 Theoretical Calculation on Species Distribution as a Function of pH

A major challenge in direct reduction for the electrochemically inert nature of phosphate lies in its inherent structure with a high enthalpy of hydration. Therefore, phosphate is often quantified indirectly via its derivatization in the molybdenum blue (MB) reaction, which is widely used for standard orthophosphate determination ²⁷. Previous studies have shown that phosphate signals can be distinguished electrochemically using macro-electrodes, where the reduction of Keggin-type PMo₁₂O₄₀⁷ anions is prevalent over the lower pH region ^{28, 29}. To better identify the phosphate content loaded by CNBC, we focused on the electrochemical behaviour of CNBC in the absence and presence of Mo (VI) across a broader pH range. Prior to electrochemical measurements at the ensemble and single-entity levels of CNBC, the speciation distribution of Mo (VI), phosphate and their complexes were simulated using Hydra/Medusa software under conditions over the pH range of 0 to 7.

As shown in Figure. 9 (a), Mo (VI) species undergo protonation and self-condensation depending on solution acidity. At pH \leq 3, dihydrogen molybdate (H₂MoO₄) mainly exhibits in the solution as a result of significant protonation and the polymerized Mo₇O₂₄⁶⁻ depolymerizes under strong acidic condition. When $3 \leq pH \leq 5$, Mo₇O₂₄⁶⁻ becomes the dominant species in solution. At pH > 5, monomeric MoO₄²⁻ predominates in the solution. Minor species such as H₃MoO₄⁺ and HMoO₄⁻ are only in small fraction. The ionization of phosphoric acid is strongly related to pH. H₂PO₄⁻ is the major species in the pH range of $2.2 \leq pH \leq 7.2$, meanwhile H₃PO₄ and HPO₄²⁻ are dominant in strongly acidic (pH < 2.2) and alkaline (pH > 7.2) conditions.

Figure. 9 (b)-(f) illustrate the speciation distribution of Mo (VI) and P in different concentration proportions with pH from 0 to 7. When $[PO_4^{3-}]$ is lower than 0.1 mM, the concentration of Mo-P complex is negligible in the system. According to Figure. 9 (e) and (f), $P_2Mo_{18}O_{62}^{6-}$ replaces $PMo_{12}O_{40}^{3-}$ as $[PO_4^{3-}]$ is higher than 0.1 mM, becoming the major Mo-P complex in the solution in strong acidic conditions (pH<3) and indicating (Eq (12)) is the dominant reaction in strong acidic solution. As $3 \le pH \le 4.5$, (Eq (13)) is the dominant equilibrium and forms the complex $PMo_{11}O_{39}^{7-}$ in abundance. However, as the proportion of $[PO_4^{3-}]$ to $[Mo\ (VI)]$ increases, $P_2Mo_5O_{23}^{6-}$ replaces $PMo_{11}O_{39}^{7-}$ as the major complex formed by Mo (VI) and P at $4.5 \le pH \le 5.5$ for the reaction of (Eq (11)). When pH > 6, Mo–P complexes are largely absent. These theoretical results provide a foundation for interpreting subsequent electrochemical experiments.

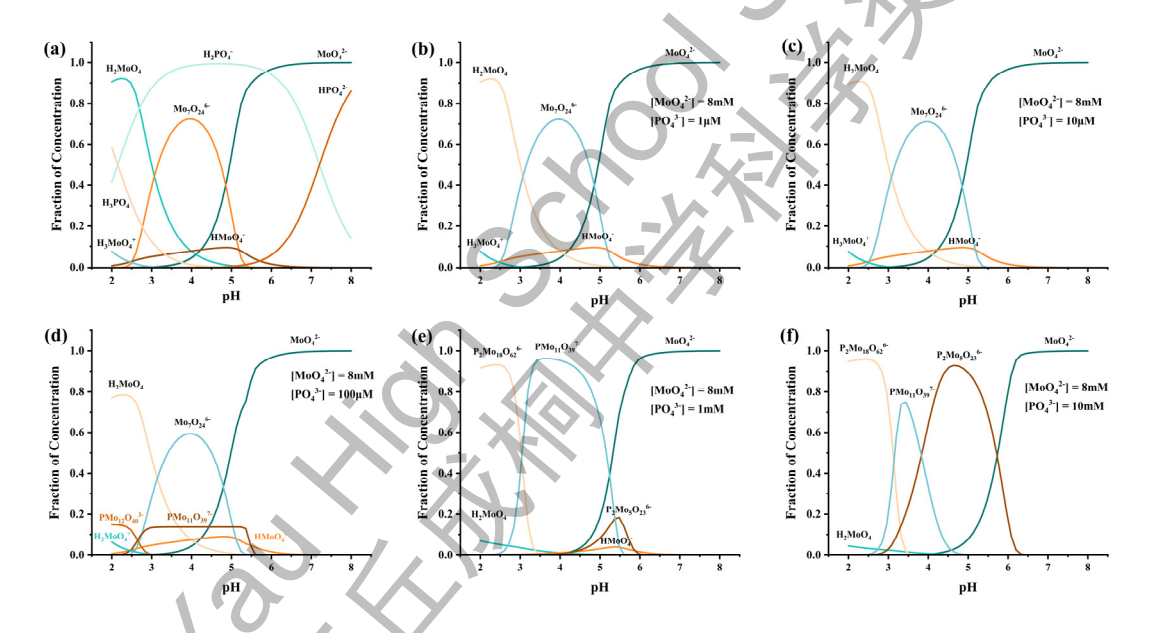


Figure. 9 Speciation distribution of molybdate ions and phosphate at different pH (a). Speciation distribution of 8 mM Mo (VI) with $[PO_4^{3-}]$ of 1 μ M, 10 μ M, 100 μ M, 1 mM and 10 mM, respectively, at different pH (b-f).

3.4 Electrochemical Behavior of Mo (VI) in the Solution Phase in CV

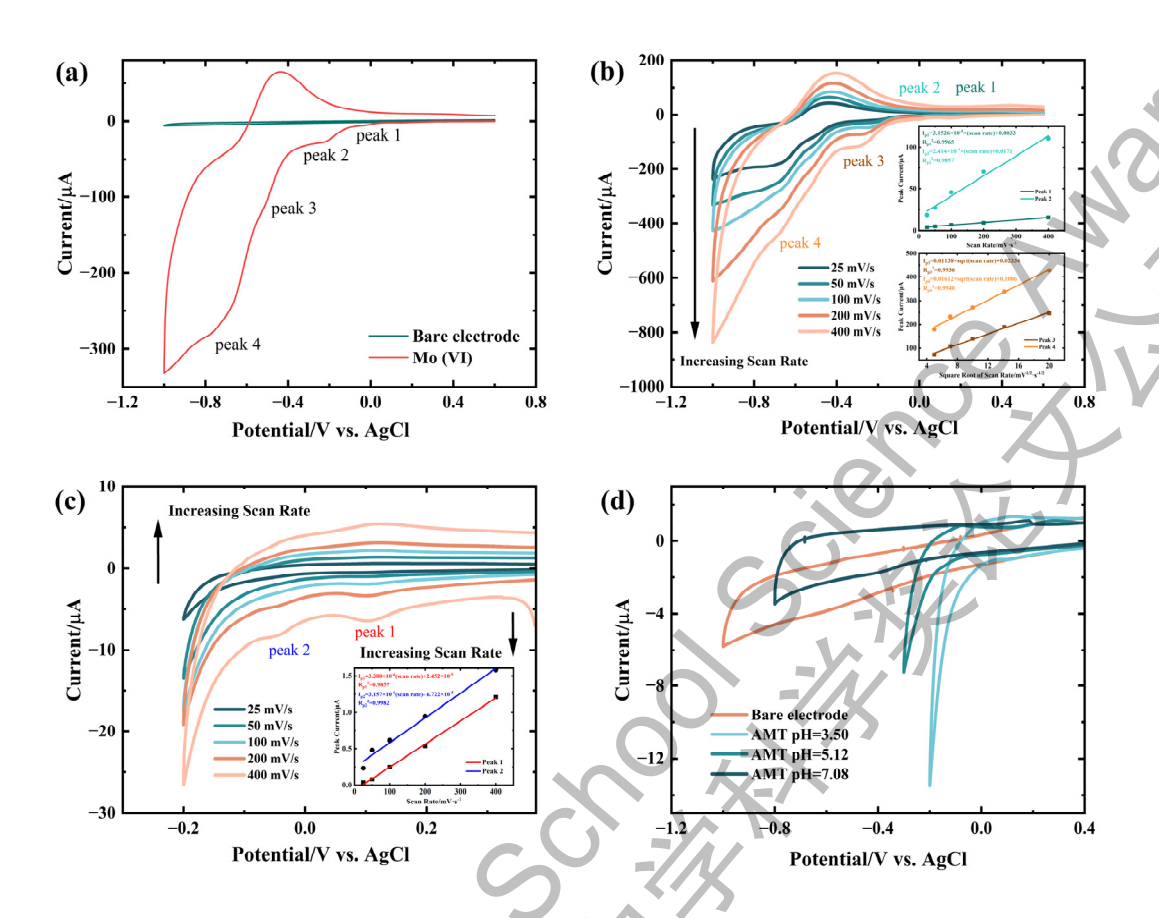


Figure. 10 (a) CV of a bare GCE in 0.05 M K_2SO_4 solution (pH = 3.50) and it in presence of 8 mM Mo (VI) at a scan rate of 50 mV/s from 0.8 V to -1.0V; (b) CV of a bare GCE in 8 mM Mo(VI)/0.05 M K_2SO_4 solution (pH = 3.50) scanned from 0.8 V to -1.0 V at a scan rate of 25, 50, 100, 200 and 400 mV/s and the linear model of peak 1, 2, 3 and 4; (c) CV of a bare GCE in 8 mM Mo(VI)/0.05 M K_2SO_4 solution (pH = 3.50) scanned from 0.6 V to -0.2 V at a scan rate of 25, 50, 100, 200 and 400 mV/s and the linear model of peak 1 and 2; (d) CV graphs at 50 mV/s of biochar-modified GCE in solution 8 mM Mo (VI)/0.05 M K_2SO_4 at pH=3.50, 5.12 and 7.08.

Following the theoretical analysis, the electrochemical behavior of bare GCE was first examined in the absence and presence of Mo (VI). Setting the scan rate of 50 mV/s through the full potential range from 0.6 V to -1.0 V, as shown in Figure. 10 (a), in 0.05 M K_2SO_4 solution without Mo (VI), no significant reduction peaks were observed. In comparison, four distinct cathodic peaks appeared at -0.01 V, -0.22 V, -0.50 V and -0.75 V respectively in the presence of Mo (VI) (pH = 3.50). In Figure. 10 (b) and (c), as the scan rate varies from 50 mV/s to 400 mV/s, the peak current of peak 1 and 2 has a positive linear relationship with scan rate ($R_1^2 = 0.9965$, $R_2^2 = 0.9857$).

Meanwhile, the peak current of peak 3 and 4 has a positive linear relationship with the square root of scan rate ($R_3^2 = 0.9936$, $R_4^2 = 0.9940$). Consequently, the reduction reactions that happened at peak 1 and 2 are under adsorption-controlled and those that happened at peak 3 and 4 is under diffusion-controlled. The valence states of the Mo-based redox couples involved in the four peaks were assigned based on literature reports. Specifically, K.Chandarasekara Pillai et.al proposed that peak 4 corresponds to a solution-phase diffusion-controlled electron transfer, while peak 3 reflects adsorption effects at higher scan rates 30 . Lu et al. attributed all four peaks to stepwise $Mo(VI) \rightarrow Mo(V)$ reductions in different chemical or adsorbed states 31,32 .

In our study, an oxidation peak at -0.43 V was detected in the reverse scan in the presence of Mo (VI) with a peak-to-peak potential separation value (E_{pp}) of 0.238±0.010 V, indicating a quasi-reversible one-electron transfer process. The corresponding reduction steps can be summarized as:

$$Mo (VI)_a + e^- \rightarrow Mo (V)_{ads} peak 1$$
 (16)

$$Mo(VI)_b + e^- \rightarrow Mo(V)_{ads} peak 2$$
 (17)

Mo
$$(VI)_c + e^- \rightarrow Mo (V)_{sol}$$
 peak 3 (18)

$$Mo (VI)_d + e^- \rightarrow Mo (V)_{sol} peak 4$$
 (19)

Since peaks 1 and 2 represent surface adsorption-controlled processes, they were selected for detailed analysis of phosphate interactions with Mo(VI) at CNBC according to previous studies ^{31, 33}. Peaks 3 and 4, governed by diffusion, were attributed to the main redox processes of Mo–P complexes. Further investigation on the electrochemical behavior of Mo (VI) reduction within a narrow potential range (0.6 V to -0.2 V, 0.6 V to -0.3 V and 0.6 V to -0.8 V) corresponded to different pH values (3.5, 5.1 and 7.9) revealed that the peak potential of peaks 1 and peak 2 were observed to shift negatively as pH was increased Figure. 10 (d), consistent with proton-coupled electron transfer. The dependence follows the Nernst relationship:

$$E = E^0 - \frac{2.303 mRT}{nF} pH \tag{20}$$

where E is the observed potential, E^0 is the standard electrode potential for the reaction, m and n are the number of protons and electrons involved in the electrode reaction, respectively, R is the universal gas constant, T is the absolute temperature, F is the Faraday constant. The diminishing peak intensities with increasing pH correlate with the speciation shift toward unprotonated Mo (VI) species in agreement with the theoretical speciation distribution.

3.5 Electrochemical Identification of Surface-Bound Phosphate on CNBC

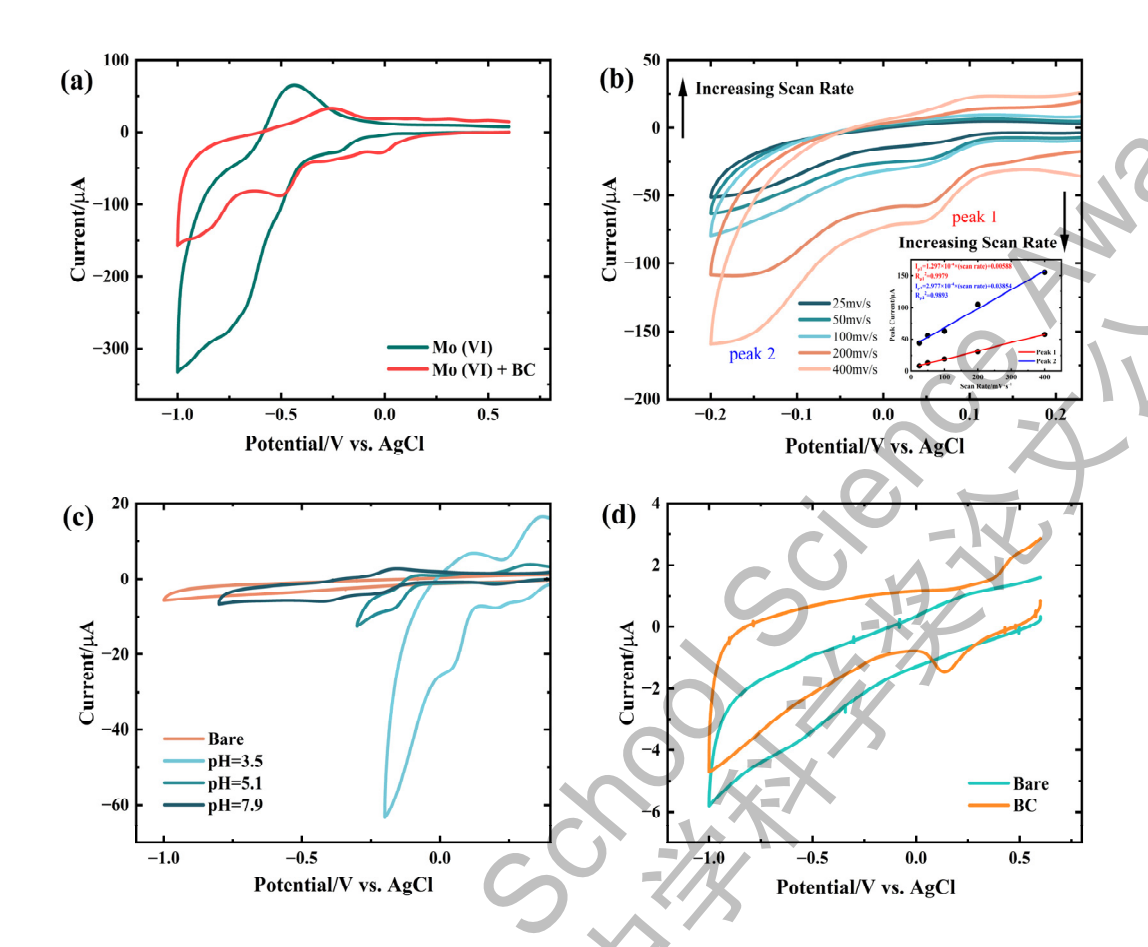


Figure 11. (a) CV of a bare GCE and a GCE modified with $8\mu L$ 2.5 g·L⁻¹ CNBC in a 8 mM Mo (VI)/0.05 M K₂SO₄ solution (pH = 3.50) at a scan rate of 50 mV/s from 0.6 V to -1.0 V; (b) CV of GCE modified with $8\mu L$ 2.5 g·L⁻¹ CNBC in a Mo (VI)/0.05 M K₂SO₄ solution (pH=3.50) scanned from 0.6 V to -0.2 V at a scan rate of 25, 50, 100, 200 and 400 mV/s and the linear model of peak 1 and 2; (c) CV of a bare CGE and a $8\mu L$ g·L⁻¹ CNBC-modified GCE in solution 8 mM Mo (VI)/0.05 M K₂SO₄ at pH = 3.50, 5.12 and 7.08 at a scan rate of 50 mV/s scanned from 0.6 V to -1.0 V, -0.2 V, -0.3 V and -0.8 V respectively; (d) CV of a bare GCE and a CGE modified with $8\mu L$ 2.5 g·L⁻¹ CNBC in a 0.05 M K₂SO₄ solution (pH = 3.50) at a scan rate of 50 mV/s from 0.6 V to -1.0 V.

To probe the reactive phosphate species loaded by CNBC, a defined amount of CNBC was immobilized on the surface of bare GCE to investigate the electrochemical performance of phosphate loaded by particles in the presence of Mo (VI). As shown in Figure. 11 (a), the CNBC-modified GCE exhibited four reduction peaks at -0.01 V, -0.23 V, -0.50 V and approximately -0.87 V, respectively. Compared with bare GCE in section 3.4, the CNBC-modified electrode produced significantly larger reduction charges (peak areas) at peaks 1 and 3, indicating that phosphate species

associated with CNBC actively participated in redox interactions with Mo (VI).

A more focused scan window (Figure. 11 (b)) revealed that peaks 1 and 2 observed at 0.05 V and -0.15 V, displayed strong positive linear relationships between peak current and scan rate $(R_1^2 = 0.9979, R_1^2 = 0.9893)$, indicating adsorption-controlled processes. This behavior confirms that the phosphate species anchored on CNBC surfaces contribute directly to electrochemical signals by forming surface-bound P-Mo (VI) complexes.

Mechanistically, the reduction of surface-associated P-Mo (VI) complexes occurs through multiple steps that can be assigned to observed peaks. Peak 1 is assigned to the one-electron reduction of the most electroactive Mo (VI) centers interacting with phosphate groups at the CNBC surface, forming Mo(V). The second cathodic peak 2 corresponds to the subsequent reduction of less accessible or more strongly bound Mo (VI) species. At more negative potentials, a pronounced increase in cathodic current is attributed to a possible surface catalytic (EC') process ³⁴. The overall process can be expressed as:

$$Mo(V)_{ads} + PMo_{12}(VI)O_{40}^{3-} \rightarrow Mo(V) + PMo_{2}(V)Mo_{10}(VI)O_{40}^{3-}$$
 (21)

$$(Mo(V)_{C})_{sol} + PMo_{2}(V)Mo_{10}(VI)O_{40}^{3-} \rightarrow (Mo(VI)_{C})_{sol} + PMo_{4}(V)Mo_{8}(VI)O_{40}^{3-}$$
(22)

The pH dependence of the electrochemical response was examined at 3.50, 5.12 and 7.08 (Figure. 11 (c)). With increasing pH, peak potential shifted negatively, consistent with proton-coupled electron transfer. In acidic solutions, both cathodic and anodic peaks in CV became more pronounced with higher currents and larger charges, reflecting enhanced accessibility and stronger binding of phosphate groups at the CNBC surface. These results indicate that acidic conditions are most favorable for revealing the active phosphate sites on CNBC.

As illustrated in Figure 13 (d), the comparison between bare and CNBC-modified GCEs highlights the significant role of CNBC. The enhanced electrochemical responses are attributed to oxygen-containing functional groups and defect sites at CNBC surfaces. These surface functionalities not only stabilize phosphate species but also promote their effective complexation with Mo(VI), thereby amplifying the redox signals. Together, these results confirm that CV of CNBC-modified electrodes provides a direct electrochemical signature of surface-active phosphate species, thereby offering a fundamental mechanism to probe the phosphate functionality carried by CNBC at single-entity level.

3.6 Electrochemical Identification of Phosphate Loaded by Single CNBC Particle

Nano impact experiments were conducted to probe the electrochemical redox behavior of CNBC via the collision of individual CNBC particles with a microelectrode held at different potentials. The representative chronoamperograms are measured at -0.6 V, -0.4 V, -0.2 V, 0 V, 0.2 V, 0.4 V and 0.6 V using a carbon micro-wire electrode saturated in 0.05 M K₂SO₄ solution with the presence of Mo (VI) and absence of Mo (VI) at pH = 1.87 (Figure. 12) firstly, respectively. As shown in Figure. 13, typical signals in chronoamperograms at each potential are selected, displaying the frequency, residence time, current charge, shape, etc. The current charge and peak height under each potential are displayed in Figure. 15, along with its distribution in Figure. 16.

Here, further research is expected to thoroughly identify the content of reactive phosphate loading on the CNBC particles at the single-entity level, based on the electrocatalytic reduction of free Mo (VI) ions with the involvement of PMo₁₂O₄₀³⁻ as described in section 3.5. As shown in Figure. 13 (a-g) and 15, the reductive steps and spikes were observed over the potential range from -0.2 V to -0.6 V at pH = 1.87. Steps occur when a CNBC particle collides with to electrode and is stably attached to the electrode surface and continues to react. Spike exhibits shortly as particles touch the electrode and quickly detach. At potential of -0.2 V, -0.4 V and -0.6 V, the average current height of reductive spikes achieved -1.03×10⁻⁸, -5.36×10⁻⁶ and -1.04×10⁻³ mA with the average charge of -4.48×10⁻⁸, -2.10×10⁻⁸ and -5.15×10⁻⁶ mC, respectively. As for the oxidative signals, extending the applied potential positive than 0 V, oxidative impacts appeared and demonstrated a potential dependency for the impact current height and charge as shown in Figure.13. At potential of 0 V, 0.2 V and 0.6 V, the average current height of oxidative spikes achieved 4.97×10^{-7} , $1.61 \times$ 10^{-6} and 1.96×10^{-5} mA with the average charge of 1.48×10^{-8} , 4.22×10^{-9} and 1.43×10^{-7} mC, respectively. It is speculated that the spikes are primarily associated with the oxidation of the CNBC themselves, possibly at edge planes and at pre-existing oxygen functionality, such as the quinone functionality inferred from previous study³⁵.

In comparison with the more acidic condition, when the pH = 4.94 (Figure.14), for the reductive signals, steps are larger at pH = 1.87 than at pH = 4.94, with longer residence time (ranging from 0.025 s to 0.4 s. As shown in Figure. 12 and 13 (h-n), the residence time is rarely more than 0.05 s at pH = 4.94, indicating a smaller charge than that at pH = 1.87. As for oxidative signals, indicated by Figure. 16, the current charge at pH = 4.94 is smaller than that at 1.87. At potential of 0.2 V, 0 V -0.2 V, -0.4 V and -0.6 V, the average current height of reductive spikes achieved -1.36×

 10^{-6} , -6.40×10^{-6} and -9.42×10^{-7} , -9.17×10^{-7} and -5.18×10^{-5} mA with the average charge of -7.44×10^{-7} , -1.99×10^{-7} and -3.01×10^{-9} , -1.68×10^{-9} and -8.76×10^{-8} mC, respectively. As for the oxidative signals, appearing mainly in 0.4 V and 0.6 V, the average current height of reductive spikes achieved 1.70×10^{-5} and 3.68×10^{-5} mA with the average charge of 4.81×10^{-8} and 1.27×10^{-7} mC, respectively.

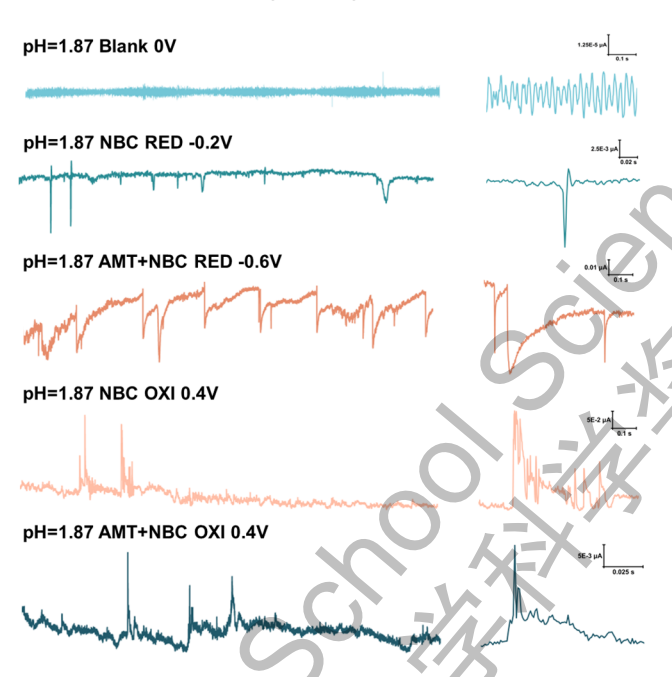


Figure. 12 Representative chronoamperograms of reductive and oxidative impact signals from the carbon micro-wire electrode saturated in 0.05 M K_2SO_4 (blank), 5 $\mu g \cdot L^{-1}$ CNBC/ 0.05 M K_2SO_4 , 4 mM Mo(VI) /5 $\mu g \cdot L^{-1}$ CNBC/ 0.05 M K_2SO_4 solution, respectively, at pH of 1.87 at -0.6 V, -0.2 V, 0 V and 0.4 V vs Ag/AgCl.

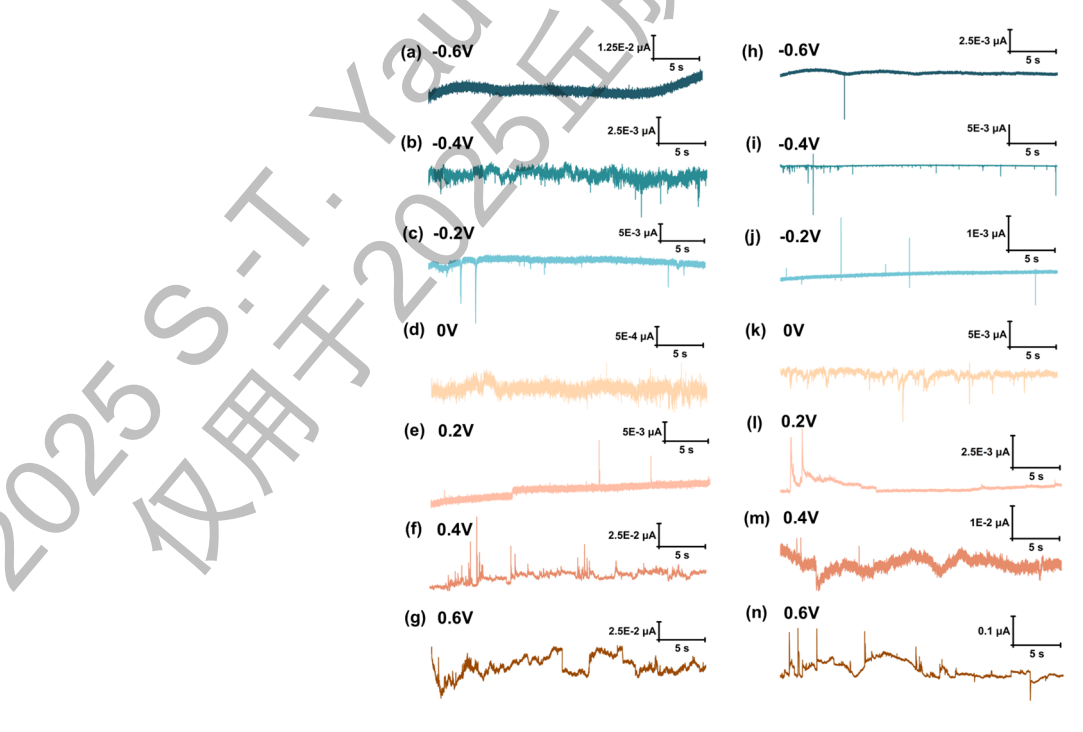


Figure. 13 Representative chronoamperograms of reductive and oxidative impact signals from the carbon micro-wire electrode saturated in 5 μ g·L⁻¹ CNBC/ 4 mM Mo(VI)/ 0.05 M K₂SO₄ solution at pH = 1.87 under potential of -0.6 V (a), -0.4 V (b), -0.2 V (c), 0 V (d), 0.2 V (e), 0.4 V (f) and 0.6 V (g); Representative chronoamperograms of reductive and oxidative impact signals from the carbon micro-wire electrode saturated in 5 μ g·L⁻¹ CNBC/ 4 mM Mo(VI)/ 0.05 M K₂SO₄ solution at pH = 4.94 under potential of -0.6 V (h), -0.4 V (i), -0.2 V (j), 0 V (k), 0.2 V (l), 0.4 V (m) and 0.6 V (n).

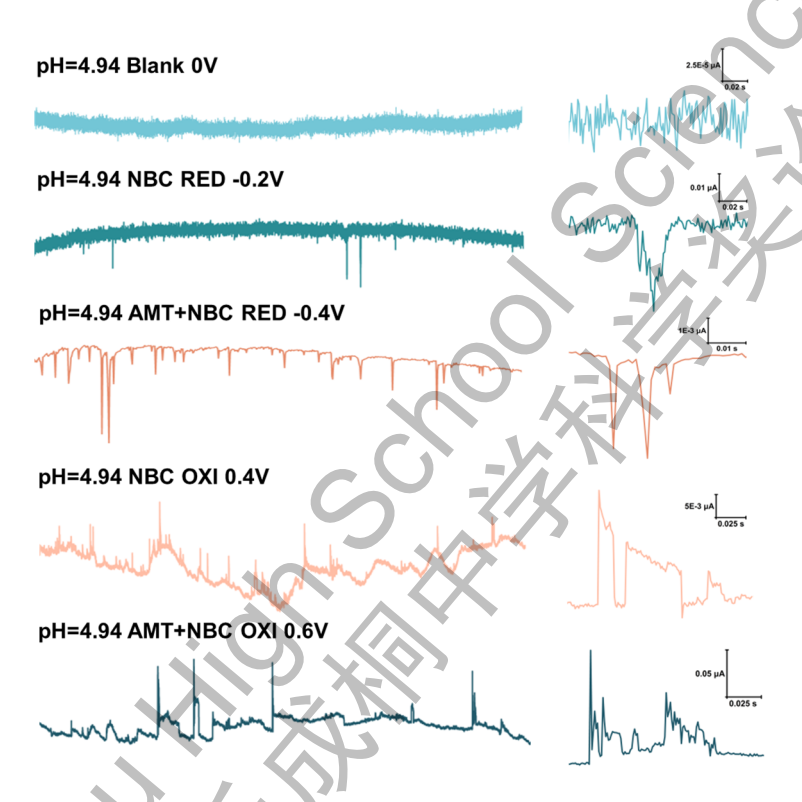


Figure. 14 Representative chronoamperograms of reductive and oxidative impact signals from the carbon micro-wire electrode saturated in 0.05 M K_2SO_4 (blank), 0.1 g·L⁻¹ CNBC/ 0.05 M K_2SO_4 , 4 mM Mo(VI)/ 0.1 g·L⁻¹ CNBC/ 0.05 M K_2SO_4 solution, respectively, at pH of 4.94 at -0.4 V, -0.2 V, 0 V, 0.4 V and 0.6 V vs Ag/AgCl.

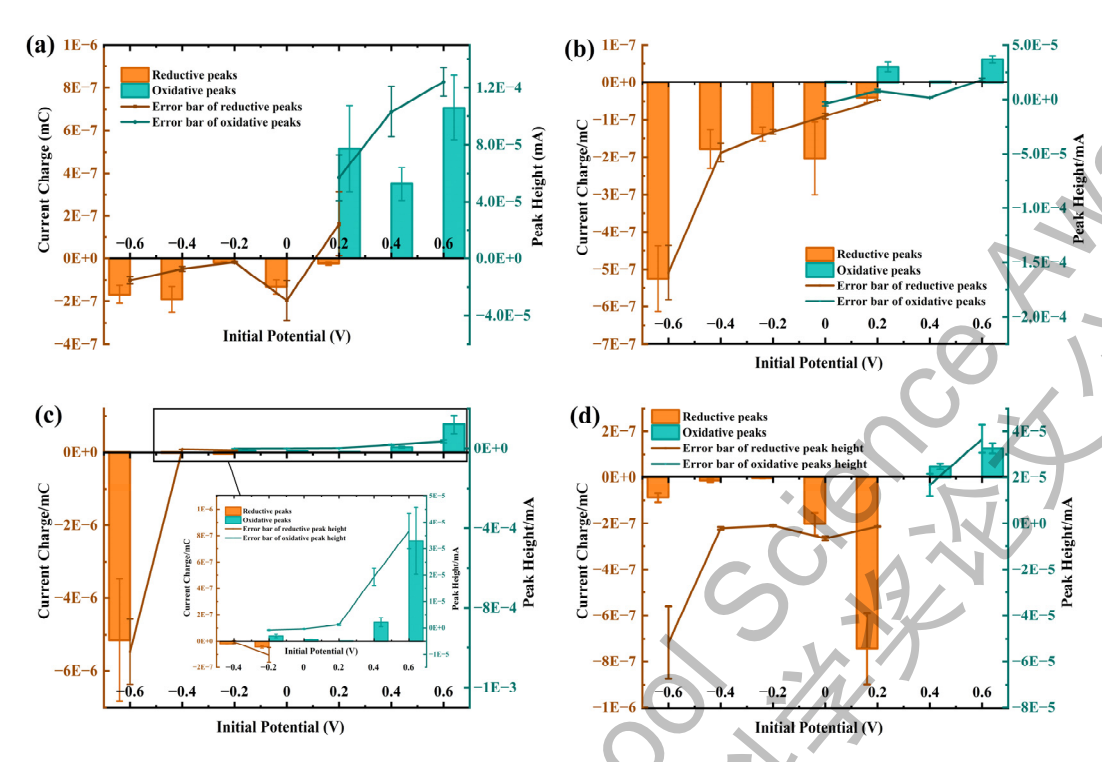


Figure. 15 Current charge and peak height of reductive and oxidative peaks at -0.6 V, -0.4 V, -0.2 V, 0 V, 0.2 V, 0.4 V and 0.6 V from the carbon micro-wire electrode saturated in 5 μ g·L⁻¹ CNBC/ 0.05 M K₂SO₄ solution at pH = 1.87 (a), 5 μ g·L⁻¹ CNBC/ 0.05 M K₂SO₄ solution at pH = 4.94 (b), 5 μ g·L⁻¹ CNBC/ 4 mM Mo (VI)/ 0.05 M K₂SO₄ solution at pH = 1.87 (c) and 5 μ g·L⁻¹ CNBC/ 4 mM Mo(VI)/ 0.05 M K₂SO₄ solution at pH = 4.94 (d).

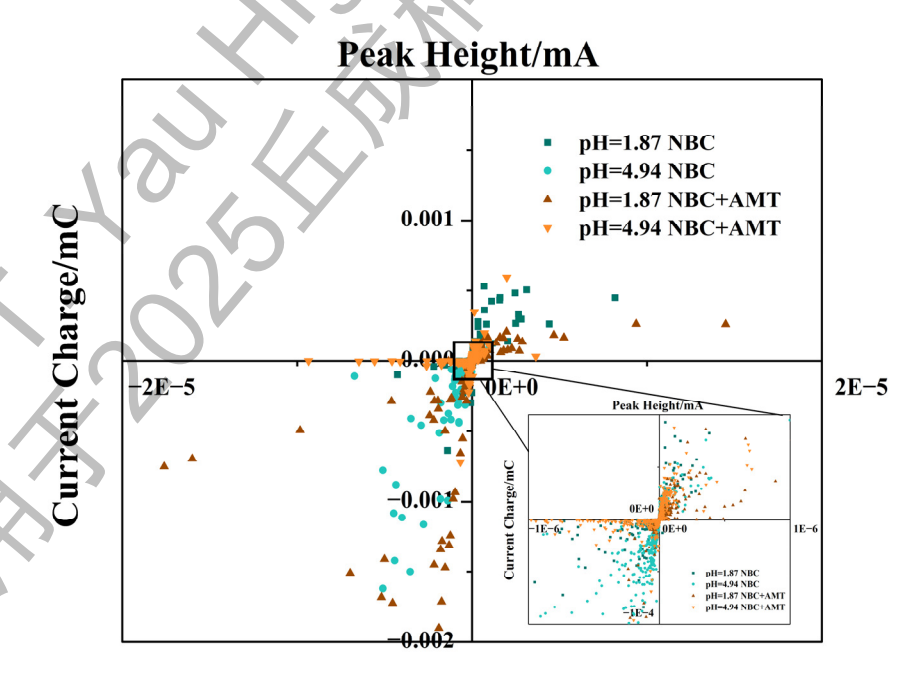


Figure 16. Current charge and height of reduction and oxidation in single entity collisions of the carbon micro-wire electrode saturated in 5 μg·L⁻¹ CNBC/ 0.05 M K₂SO₄ solution, respectively, at

pH=1.87 (dark green) and 4.94 (blue); in 5 μ g·L⁻¹ CNBC/ 0.05 M K₂SO₄ solution at pH=1.87 (brown) and 4.94 (orange).

Electrochemical measurements of CNBC at single-particle level under acidic and close to neutral pH conditions in the presence or absence of Mo(VI) revealed distinct distributions of peak charge and peak height as shown in Figure.16. Most oxidative and reductive peaks exhibited heights below 10⁻⁵ mA and charges smaller than 0.001 mC, indicating that the active sites of CNBC are not uniform but instead span a wide energy distribution, consisting of a few strong binding sites and many weak ones. This heterogeneity arises from nanoscale size effects and surface functionality. Smaller CNBC particles, with their larger specific surface areas and more abundant defect sites, exhibit higher activity and faster phosphate release rates. Moreover, the binding of phosphate strongly depends on the protonation state of oxygen-containing surface groups (–OH, –COOH, –C=O). Under acidic conditions, protonation enhances electrostatic attraction and hydrogen bonding, strengthening phosphate adsorption and producing stronger electrochemical responses. At nearneutral or alkaline pH, deprotonation reduces these interactions, leading to weaker retention. Thus, CNBC-phosphate interactions are governed not only by bulk composition but also by particle size, morphology, and pH-dependent surface chemistry.

Conventional ensemble electrochemical techniques average out this variability, obscuring the contribution of individual particles and preventing mechanistic insight into strongly bound, weakly bound, and dynamically exchanging phosphate species. In contrast, SECE directly captures the stochastic collisions of individual nanoparticles with an electrode, enabling quantification of their phosphate loading and binding behaviors. Therefore, the results above uncover the distribution of active sites, particle-to-particle heterogeneity, and the role of size and surface chemistry in phosphate redox activity—providing mechanistic insights inaccessible through bulk methods. Ultimately, SECE complements ensemble methods by revealing the intrinsic heterogeneity of CNBC—phosphate systems, thereby offering a more fundamental understanding of their role in controlled nutrient release and environmental applications.

4. Environmental Implications

From an environmental perspective, the relatively weak intermolecular interactions between phosphate and CNBC make the material an ideal candidate for slow-release fertilizers. Negatively

charged oxygen-containing surface groups not only regulate phosphate retention but also attract Ca²⁺, thereby stabilizing phosphate in soil while ensuring gradual nutrient release. Unlike conventional fertilizers, which often cause rapid nutrient loss and environmental contamination, CNBC ensures a steady phosphorus supply that matches plant growth requirements. The low cost of *Canna indica* as a powerful source of NBC further adds future possibility of large-scale application for this environmentally-friendly fertilizer. The waste straws of plants like *Canna indica* could be collected, processed and utilized as a sustainable resource in agriculture, which reveals more prospects of zero-chemical-fertilizer recyclable farmland management, saving cost while protecting the environment.

Most of all, this approach aligns closely with China's national goals and its emphasis on green, low-carbon, and sustainable agriculture. The use of crop residues such as Canna indica for biochar production directly contributes to carbon sequestration (固碳) by stabilizing biomass carbon in soils, while simultaneously reducing greenhouse gas emissions from open burning of straw. Moreover, it echoes the strategic direction of policies such as the Rural Revitalization Strategy (乡村振兴战略) ³⁶, the Zero-Growth Action Plan for Fertilizer Use (化肥零增长行动计划) ³⁷, and the 14th Five-Year Plan for Green Agriculture (十四五绿色农业发展规划) ³⁸, all of which encourage resource recycling, chemical fertilizer reduction, and eco-friendly farming practices.

Therefore, NBC not only offers a sustainable path for phosphorus management in agriculture but also serves as a practical technology supporting China's transition toward a low-carbon, circular, and environmentally resilient agricultural system.

5. Conclusions

The negative impact of nutrient runoff and water eutrophication caused by conventional chemical fertilizers raises demand for more environmentally friendly P fertilizer at low costs. In this work, an investigation into the macro and micro electrochemical properties of NBC derived from *Canna indica* indicates its strong P slowly-release capacity in dynamic binding sites associated with particle size and pH. Containing more metal ions and oxygen-containing groups compared with NBC derived from corn stalks, CNBC more effectively detects phosphate and attracts, and this effect is more significant as pH decreases, as CV and DFT calculations imply. The particle heterogeneity in the CNBC-phosphate system revealed by SECE shows binding sites in multiple current charge

and height, with most in labile adsorption sites and some in stable adsorption controlled by electrostatic attraction between C-O, C=O, -OH, etc, and positive ions Ca²⁺ and phosphate. The slow-release property of CNBC and NBC derived from other plants and agricultural waste marks future application potential for sustainable resource utilization in farmland management. The different functional modification on the edge of NBC is also expected to adjust its fixation or release effect of P.

Reference

- (1) Lambers, H. Phosphorus Acquisition and Utilization in Plants. *Annu Rev Plant Biol* **2022**, *73*, 17-42. DOI: 10.1146/annurev-arplant-102720-125738.
- (2) Yang, S.-Y.; Lin, W.-Y.; Hsiao, Y.-M.; Chiou, T.-J. Milestones in understanding transport, sensing, and signaling of the plant nutrient phosphorus. *The Plant Cell* **2024**, *36* (5), 1504-1523. DOI: 10.1093/plcell/koad326 (accessed 9/13/2025).
- (3) Carpenter, S. R.; Caraco, N. F.; Correll, D. L.; Howarth, R. W.; Sharpley, A. N.; Smith, V. H. NONPOINT POLLUTION OF SURFACE WATERS WITH PHOSPHORUS AND NITROGEN. *Ecological Applications* **1998**, 8 (3), 559-568. DOI: https://doi.org/10.1890/1051-0761(1998)008[0559:NPOSWW]2.0.CO;2.
- (4) Huang, J.; Xu, C.-c.; Ridoutt, B.; Wang, X.-c.; Ren, P.-a. Nitrogen and phosphorus losses and eutrophication potential associated with fertilizer application to cropland in China. *Journal of Cleaner Production* **2017**, *159*. DOI: 10.1016/j.jclepro.2017.05.008.
- (5) Du, Y.; Li, T.; He, B. Runoff-related nutrient loss affected by fertilization and cultivation in sloping croplands: An 11-year observation under natural rainfall. *Agriculture, Ecosystems & Environment* **2021**, 319, 107549. DOI: https://doi.org/10.1016/j.agee.2021.107549.
- (6) Ji, X. Y.; Hou, H. H.; Wang, S. S.; Yang, K. [Variation Characteristics of Surface Water Quality in China in Recent Years]. *Huan Jing Ke Xue* **2022**, *43* (10), 4419-4429. DOI: 10.13227/j.hjkx.202111299.
- (7) Wang, C.; Luo, D.; Zhang, X.; Huang, R.; Cao, Y.; Liu, G.; Zhang, Y.; Wang, H. Biochar-based slow-release of fertilizers for sustainable agriculture: A mini review. *Environ Sci Ecotechnol* **2022**, *10*, 100167. DOI: 10.1016/j.ese.2022.100167.
- (8) Joshi, M.; Bhatt, D.; Srivastava, A. Enhanced Adsorption Efficiency through Biochar Modification: A Comprehensive Review. *Industrial & Engineering Chemistry Research* **2023**, *62* (35), 13748-13761. DOI: 10.1021/acs.iecr.3c02368.
- (9) Shafiq, F.; Anwar, S.; Firdaus-e-Bareen; Zhang, L.; Ashraf, M. Nano-biochar: Properties and prospects for sustainable agriculture. *Land Degradation & Development* **2023**, *34* (9), 2445-2463. DOI: https://doi.org/10.1002/ldr.4620.
- (10) Deng, L.; Tu, P.; Ahmed, N.; Zhang, G.; Cen, Y.; Huang, B.; Deng, L.; Yuan, H. Biochar-based phosphate fertilizer improve phosphorus bioavailability, microbial functioning, and citrus seedling growth. *Scientia Horticulturae* **2024**, *338*, 113699. DOI: https://doi.org/10.1016/j.scienta.2024.113699. (11) Gao, S.; DeLuca, T. H.; Cleveland, C. C. Biochar additions alter phosphorus and nitrogen availability in agricultural ecosystems: A meta-analysis. *Science of The Total Environment* **2019**, *654*, 463-472. DOI:

https://doi.org/10.1016/j.scitotenv.2018.11.124.

- (12) Nobaharan, K.; Bagheri Novair, S.; Asgari Lajayer, B.; van Hullebusch, E. D. Phosphorus Removal from Wastewater: The Potential Use of Biochar and the Key Controlling Factors. *Water* **2021**, *13* (4), 517.
- (13) Jin, J.; Fang, Y.; Liu, C.; Eltohamy, K. M.; He, S.; Li, F.; Lu, Y.; Liang, X. Reduced colloidal phosphorus release from paddy soils: A synergistic effect of micro-/nano-sized biochars and intermittent anoxic condition. *Science of The Total Environment* **2023**, *905*, 167104. DOI: https://doi.org/10.1016/j.scitotenv.2023.167104.
- (14) Kalu, O.; Ariaga, C. A. Nutritional Evaluation of Various Parts of Canna indica L. *Annual Research & Review in Biology* **2016**, *11*, 1-5. DOI: 10.9734/ARRB/2016/31029.
- (15) Dai, L.; Tan, F.; Wu, B.; He, M.; Wang, W.; Tang, X.; Hu, Q.; Zhang, M. Immobilization of phosphorus in cow manure during hydrothermal carbonization. *J Environ Manage* **2015**, *157*, 49-53. DOI: 10.1016/j.jenvman.2015.04.009.
- (16) Gao, S.; DeLuca, T. Influence of Biochar on Soil Nutrient Transformations, Nutrient Leaching, and Crop Yield. *Advances in Plants & Agriculture Research* **2016**, **4**, 00150. DOI: 10.15406/apar.2016.04.00150.
- (17) Yang, L.; Wu, Y.; Wang, Y.; An, W.; Jin, J.; Sun, K.; Wang, X. Effects of biochar addition on the abundance, speciation, availability, and leaching loss of soil phosphorus. *Science of The Total Environment* **2021**, 758, 143657. DOI: https://doi.org/10.1016/j.scitotenv.2020.143657.
- (18) Chen, L.; Huang, X.; Sun, S.; Zhuo, Y.; Li, C.; Sun, C. An effective biochar-based slow-release fertilizer for promoting the formation of bioavailable P-phase and the slow-release performance of nutrients by the addition of attapulgite. *Journal of Environmental Chemical Engineering* **2025**, *13* (5), 118240. DOI: https://doi.org/10.1016/j.jece.2025.118240.
- (19) Edwards, M. A.; Robinson, D. A.; Ren, H.; Cheyne, C. G.; Tan, C. S.; White, H. S. Nanoscale electrochemical kinetics & dynamics: the challenges and opportunities of single-entity measurements. *Faraday Discussions* **2018**, *210* (0), 9-28, 10.1039/C8FD00134K. DOI: 10.1039/C8FD00134K.
- (20) Sekretareva, A. Single-entity electrochemistry of collision in sensing applications. *Sensors and Actuators Reports* **2021**, *3*, 100037. DOI: https://doi.org/10.1016/j.snr.2021.100037.
- (21) HYDRA (Hydrochemical Equilibrium- Constant Database) and MEDUSA (Make Equilibrium Diagrams Using Sophisticated Algorithms) Programs Royal Institute of Technology, Sweden., 2004. http://www.ke-mi.kth.se/medusa (accessed.
- (22) You, J.; Wu, D.; Liu, H. Electrochemical studies of molybdate and thiomolybdates. *Polyhedron* **1986**, *5* (1), 535-537. DOI: https://doi.org/10.1016/S0277-5387(00)84960-8.
- (23) Grimme, S. Density functional theory with London dispersion corrections. *WIREs Computational Molecular Science* **2011**, *I* (2), 211-228. DOI: https://doi.org/10.1002/wcms.30.
- (24) Zhao, N.; Lv, Y.; Yang, X. A new 3D conceptual structure modeling of biochars by molecular mechanic and molecular dynamic simulation. *Journal of Soils and Sediments* **2017**, *17* (3), 641-655. DOI: 10.1007/s11368-015-1308-y.
- (25) Zhou, Z.; Lu, M.; Huang, Y.; Zhao, C.; Wang, Y.; Pidou, M.; Wu, M.; Chen, Q.; Jeffrey, P.; Pan, B. Molecular mechanistic insights towards aggregation of nano-biochar moderated by aromatic components in dissolved organic matter. *Environment International* **2025**, *197*, 109350. DOI: https://doi.org/10.1016/j.envint.2025.109350.
- (26) Wood, R.; Mašek, O.; Erastova, V. Developing realistic molecular models of biochars. *Cell Reports Physical Science* **2024**, *5* (7), 102037. DOI: https://doi.org/10.1016/j.xcrp.2024.102037.

- (27) Nagul, E. A.; McKelvie, I. D.; Worsfold, P.; Kolev, S. D. The molybdenum blue reaction for the determination of orthophosphate revisited: Opening the black box. *Analytica Chimica Acta* **2015**, *890*, 60-82. DOI: https://doi.org/10.1016/j.aca.2015.07.030.
- (28) Kolliopoulos, A. V.; Kampouris, D. K.; Banks, C. E. Rapid and Portable Electrochemical Quantification of Phosphorus. *Analytical Chemistry* **2015**, *87* (8), 4269-4274. DOI: 10.1021/ac504602a.
- (29) Wang, H.; Hamanaka, S.; Nishimoto, Y.; Irle, S.; Yokoyama, T.; Yoshikawa, H.; Awaga, K. In Operando X-ray Absorption Fine Structure Studies of Polyoxometalate Molecular Cluster Batteries: Polyoxometalates as Electron Sponges. *Journal of the American Chemical Society* **2012**, *134* (10), 4918-4924. DOI: 10.1021/ja2117206.
- (30) Pillai, K.; Ilangovan, G. Cyclic voltammetric studies on electroreduction of Mo(VI) on GC electrodes. *Bulletin of Electrochemistry* **1993**, *9*, 592-595.
- (31) Lu, Y.; Li, X.; Li, D.; Compton, R. G. Amperometric Environmental Phosphate Sensors. *ACS Sensors* **2021**, *6* (9), 3284-3294. DOI: 10.1021/acssensors.1c01035.
- (32) Lu, Y.; Ma, T.; Zhang, M.; Lan, Q.; Yang, J.; Liang, X. Portable Paper-Based Sensing Platform for Rapid and Simultaneous Measurement of Environmental pH and Soluble Reactive Phosphorus. *ACS Sensors* **2025**, *10* (6), 4658-4668. DOI: 10.1021/acssensors.5c01052.
- (33) Ilangovan, G.; Chandrasekara Pillai, K. Electrochemical and XPS Characterization of Glassy Carbon Electrode Surface Effects on the Preparation of a Monomeric Molybdate(VI)-Modified Electrode. *Langmuir* **1997**, *13* (3), 566-575. DOI: 10.1021/la960053n.
- (34) Unoura, K.; Tanaka, N. Comparative study of the electrode reactions of 12-molybdosilicate and 12-molybdophosphate. *Inorganic Chemistry* **1983**, *22* (20), 2963-2964. DOI: 10.1021/ic00162a042.
- (35) Lu, Y.; Li, X.; Compton, R. G. Oxygen Reduction Reaction at Single Entity Multiwalled Carbon Nanotubes. *The Journal of Physical Chemistry Letters* **2022**, *13* (16), 3748-3753. DOI: 10.1021/acs.jpclett.2c00871.
- (36) 农业农村部关于加快农业发展全面绿色转型促进乡村生态振兴的指导意见.国务院部门文件,2024.中国政府网 www.gov.cn/zhengce/zhengceku/202412/content 6995343.htm
- (37) 种植业管理司. "农业农村部关于印发《到 2025 年化肥减量化行动方案》和《到 2025 年化 学 农 药 减 量 化 行 动 方 案 》 的 通 知." Moa.gov.cn, 2025, www.moa.gov.cn/govpublic/ZZYGLS/202212/t20221201 6416398.htm.
- (38) "农业农村部 国家发展改革委 科技部 自然资源部 生态环境部 国家林草局关于印发《"十四五"全国农业绿色发展规划》的通知_国务院部门文件_中国政府网." Www.gov.cn, 2021, www.gov.cn/zhengce/zhengceku/2021-09/07/content 5635867.htm

Appendix

Working Electrode Preparation and Characterization (after 2.2)

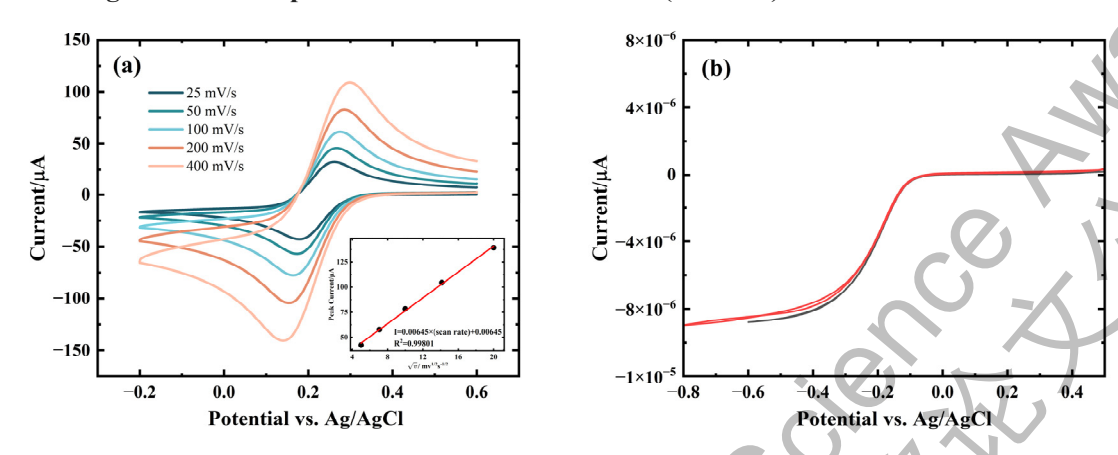


Figure. 17 (a) CV curves of macroelectrode GCE in 5 mM K_3 [FeCN₆] / 0.1 M KCl solution at scan rates from 25 to 50, 100, 200, 400 mV/s vs. Ag/AgCl; (b) CV curve of CFE in 5 mM K_3 [FeCN₆] / 0.1 M KCl solution at a scan rate of 5 mV/s vs. Ag/AgCl.

The polished GCE and CFE were respectively characterized using CV in a 5 mM potassium ferricyanide (K₃[Fe(CN)₆]) solution containing 0.1 M potassium chloride (KCl). Different scan rates from 25 mVs⁻¹ to 50, 100, 200, and 400 mVs⁻¹ were set in turn to obtain the voltametric curves of bare GCE. As shown in Figure.2 (a), a reduction peak at 0.164 ± 0.0161 V and an oxidation peak at 0.277 ± 0.0152 V were observed, respectively. According to the Randles-Sevcik equation, the strong, positive linear relationship between the peak current and the square root of the scan rate (R²=0.9980) proved that this electrochemical reaction is electrochemically reversible and under diffusion-controlled. Differently, the CV of CFE at a scan rate of 5 mV/s displayed a sigmoidal shape without well-defined peak shapes, characteristic of rapid steady-state current establishment was due to the dominant spherical diffusion at microelectrodes.

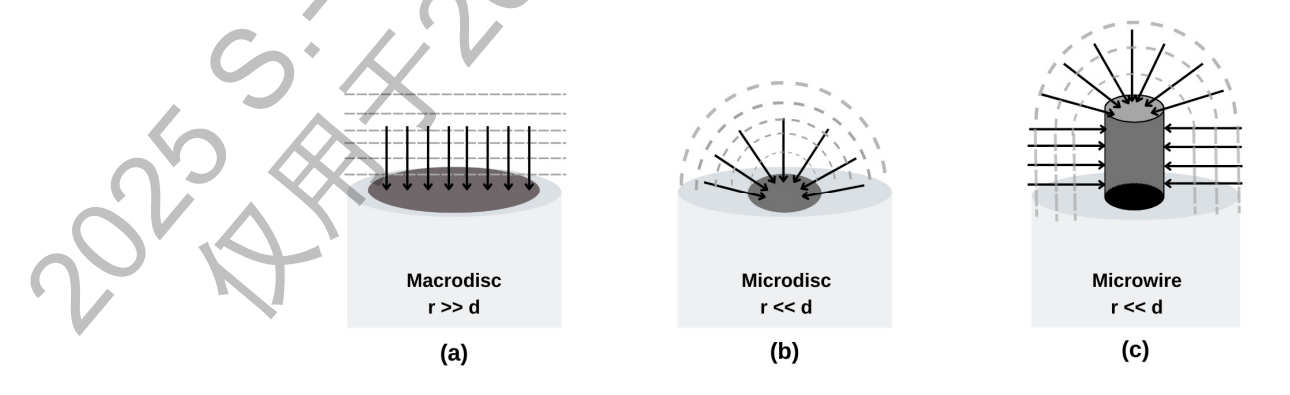


Figure.18 Diffusion model of macro-disc (a), micro-disc (b), and micro-wire (c) electrode.

Different diffusion patterns resulting from different sizes of radius of electrode and thickness of diffusion layer are shown in Figure. 3. For macrodisc electrode ($r_e \gg d$), linear diffusion leads to lower efficiency of mass transport, thus marking significant reduction and oxidation peaks (Figure.3(a)). In contrast, for microdisc and microwire electrode ($r_e \ll d$), convergent diffusion increases the rates of mass transport and replaces distinctive peaks with a steady sigmoidal shape, as Figure.3(b) shows. In particular, the cylindrical microwire electrode (Figure.3(c)) has a larger surface area, allowing for nano-impact collisions than the other two patterns of electrodes, which include both convergent and linear diffusion. Thus, its highest mass transport rate renders it most suitable for the measurement of faster electrode kinetics during single-entity collisions.

Acknowledgement 致谢

指导老师杨颖老师是我的校内化学老师,负责国际部拔尖课程项目和竞赛培训并教授 我电化学相关的拔高课程。卢圆圆老师为本研究提供了无偿指导。

在我上小学时,我的老家浙江嘉兴的水土流失和水质富营养化逐渐加重,后来"五水共治"等政策使环境逐渐好转。在高中环境科学课程的学习中,我对农业和水体环境的污染治理产生了兴趣并开始展开了研究。2025 年 3 月,我了解到浙江大学在嘉兴有部分农田有针对面源污染的氮磷生态拦截沟渠建设和试验(如下图)。我联系了项目课题组的负责人卢圆圆老师并和她介绍了我之前有关碳纳米材料的环境化学研究。就这样,我很幸运地在暑假进入课题组实验室,展开对纳米生物炭对土壤磷素缓释作用的研究,该材料在电化学的宏观微观以及理论计算的验证下,有望实现绿色农业中对如美人蕉、玉米秸秆等废弃物的资源化利用。



该研究课题是在我学习电化学基本原理、阅读课题组论文及相关文献后基于我先前在 后备人才计划的研究方向与卢圆圆老师和她在浙江大学的导师梁新强教授讨论形成。实验、 计算、数据分析及论文写作由我独立完成。卢圆圆老师在项目中为我提供了选题、实验操 作、论文修改等方面的无偿指导。红外光谱、XPS 等材料表征送检至校外检测中心完成。 单颗粒碰撞实验的碳纤维电极制作部分接受了来自课题组张梦欢师姐的指导和帮助。杨颖 老师为我的论文修改以及先前的知识学习提供了指导。由于我在之前的科研项目对 DFT 计 算有所学习和应用,在与指导老师的沟通过下,我也把量子计算作为此课题研究方法的一部分。

在此由衷感谢卢圆圆老师、梁新强教授、杨颖老师和课题组师兄师姐在研究过程中提供的宝贵帮助。